

**THE IMPROVEMENT OF IN VIVO XRF
LEAD MEASUREMENT SYSTEM**

by

Nie, Huling, B.Sc.

A Thesis

Submitted to the School of Graduate Studies

for the Degree

Master of Science

McMaster University

© Copyright by Nie, Huling, August, 2001

MASTER OF SCIENCE (2000)
(Physics and Astronomy)

McMaster University
Hamilton, Ontario

TITLE: The Improvement of In vivo XRF Lead Measurement System

AUTHOR: Nie, Huiling

SUPERVISOR: Dr. David R. Chettle

NUMBER OF PAGES: ix, 74

ABSTRACT

^{109}Cd induced K-XRF has been used for in vivo lead measurement for about two decades. The improvement of this system has been emphasized recently due to the increasing understanding of the low level lead exposure. In this work, a cloverleaf detector system is used to improve the minimum detectable limit (MDL) for the in vivo measurement of lead in bone. This system consists of four 8mm radius detectors which are placed closely with a space of 2mm between neighboring ones. We measured some bare phantoms and phantoms in leg phantom which simulates the in vivo measurement and found that the MDL is greatly improved by using the cloverleaf system and a stronger source. The effect of the geometries is also discussed. An overall MDL ratio of about 0.278 is obtained by using the cloverleaf system compared to the conventional system for the in vivo measurement, which means a decreasing of MDL from about 10 micro g/(g bone mineral) to about 2.78 micro g/(g bone mineral).

Two sets of phantoms also have been investigated due to the different calibration lines for these two sets of phantoms for the same lead measurement system. The results indicate that the compositions of these two sets of phantoms, which are supposedly the same, are greatly different. Since they were both made of "plaster of Paris", we can conclude that not all the plaster of Paris has the same composition. Hence the materials need to be measured before they are used to make the calibration phantoms.

ACKNOWLEDGEMENTS

My greatest gratitude goes to my supervisor Dr. David Chettle, for his continuous guidance, encouragement and support throughout past year, for his concern, consideration, and necessary strictness, especially for discovering so many of my merits that I don't even know for myself, and for covering so much for me. I'm very glad that I may have chance to continue my research under his supervision.

My gratitude also goes to my supervisory committee members: to Dr. Fiona McNeill, for setting a good example by her own action to show me how to be an excellent instructor, an outstanding scientist, as well as a kind friend for all the surrounding people; to Dr. Bill Prestwich, for his patience to answering all my questions and for the help in my hour of need; to Dr. Colin Webber, for his cheerful lectures as well as his great sense of humour.

I am very grateful to Dr. Michelle Arnold for all her help and encouragement in research and in life throughout past year. I also would like to thank Dr. Ian Stronach for instructing me to a lot new knowledge especially to the fitting program which has been used extensively in my research.

I would like to thank Ryan Studinski, Aslam Aslam, Sean Carew and Rao Khan for playing game and having fun together.

Last, but not the least, I would like to take this opportunity to thank my husband Baozeng, for his love and care.

TABLE OF CONTENTS

Abstract	iii
Acknowledgements	iv
Table of Contents	v
List of Figures	vii
List of Tables	viii
Chapter 1: Introduction	1
1.1 History of Lead	1
1.2 The Effects of Lead on Human Health	2
1.2.1 Neurological Effects	2
1.2.2 Haematologic Effects	3
1.2.3 Renal Effects	3
1.2.4 Reproductive and Developmental Effects	4
1.2 Lead Metabolism in Human Body	4
1.4 X-ray Fluorescence	5
1.4.1 Interactions of Photons with Specimen	5
1.4.2 In vivo X-ray Fluorescence Measurement of Lead in Bone	7
1.5 In vivo XRF Lead Measurement System Used in the Project	10
1.6 Brief Introduction of the Thesis	11
Chapter 2: A study of MDL Improvement for the In vivo Measurement of lead in Bone	12
2.1 Introduction	12
2.2 System Setup	13
2.2.1 Standard System	13
2.2.1 Cloverleaf System	14
2.3 Monte Carlo Simulation	18
2.3.1 Principle	19
2.3.2 MDL Calculation for the MC simulation	20
2.3.3 Monte Carlo Setups	21
2.3.4 Monte Carlo Simulation Results	22
2.4 Measurement Results	26
2.4.1 Data Analysis	26

2.4.2 Measurement Results	27
2.4.2.1 The Effect of Scattering, Spacing and Detector Radius	28
2.4.2.2 The Comparison of the Measurement Results	31
2.4.2.3 Geometry Effect	36
2.4.2.4 Comparison of the results for the Monte Carlo Simulation and the measurement	37
2.5 Discussion	39
Chapter 3: An investigation of ¹⁰⁹Cd KXRF Lead Measurement Calibration	44
3.1 Introduction	44
3.2 Spectrum Fitting	46
3.2.1 Coherent Fitting	47
3.2.2 Alpha Fitting	52
3.2.3 Beta Fitting	53
3.3 The Calibration Line for Old and New Phantoms	56
3.4 The Composition of the New Phantoms	59
3.4.1 The Results from the Fitting Program	59
3.4.2 The Results of Neutron Activation Analysis (NAA)	60
3.4.3 The Results of Guelph Chemical Laboratories LTD.	62
3.5 How Resolution Affects the Ca (S) edge	64
3.5.1 Relationship between Resolution and Ca edge/(Coh Area)	64
3.5.2 Relationship between Resolution and Ca edge/(Coh peak*FWHM)	66
3.6 Results for Bare Bone	68
3.7 Discussion	70
Chapter 4: Conclusion	71
4.1 Conclusion for the Improvement of the in vivo Lead Measurement System	71
4.2 Conclusion for the Lead Measurement Calibration	71
4.3 Future Work	72
References	73

List of figures

Figure 1-1	The lead XRF spectrum	10
Figure 2-1	The detector system setup	14
Figure 2-2	The horizontal cross-section of the cloverleaf detectors	15
Figure 2-3	The geometry of the standard system	16
Figure 2-4	Geometry of old phantom in leg phantom	18
Figure 2-5	Comparison of the spectrum (log scale) for Monte Carlo simulation and the measurement at energy 58keV to 88keV	22
Figure 2-6	Comparison of the spectrum (log scale) for Monte Carlo simulation and the measurement at energy 71keV to 88keV	23
Figure 3-1	The beta calibration lines for old and new phantoms	57
Figure 3-2	Ca edge/Coh peak versus resolution	66
Figure 3-3	Ca edge/(Coh peak*FWHM) versus resolution	68
Figure 3-4	The positions of the bare bone	68

LIST OF TABLES

Table 2-1	Input parameters for the Monte Carlo simulation	22
Table 2-2	Comparison of the counts in related areas obtained from Monte Carlo simulation and measurement for the 25 mm radius detector and 200 ppm lead concentration	24
Table 2-3	Normalized, geometrical and overall MDL ratios for bare bone by MC simulation	24
Table 2-4	Normalized, geometrical and overall MDL ratios for bone in soft tissue by MC simulation	25
Table 2-5	Normalized MDL ratios for cloverleaf system and standard system for bare bone by MC simulation	25
Table 2-6	Normalized MDL ratios for cloverleaf system and standard system for bone in soft tissue by MC simulation	25
Table 2-7	Ratio of MDL for 2 mm and 13 mm spacing for 8 mm and 12.5 mm detectors	29
Table 2-8	Ratio of MDL for 8 mm and 12.5 mm radius detectors with 2 mm and 13 mm spacing	30
Table 2-9	MDL ratios for cloverleaf and modified standard system for new bare phantoms	32
Table 2-10	Normalized MDL ratios for cloverleaf and modified standard system for new bare phantoms	33
Table 2-11	MDL ratios for cloverleaf and modified standard system for old phantoms in leg phantom	33
Table 2-12	Normalized MDL ratios for cloverleaf and modified standard system for old phantoms in leg phantom	34
Table 2-13	MDL ratios for cloverleaf and standard system for new bare phantoms	35
Table 2-14	Normalized MDL ratios for cloverleaf and standard system for new bare phantoms	35
Table 2-15	MDL ratios for cloverleaf and standard system for old phantoms in leg phantom	35

Table 2-16	Normalized MDL ratios for clover and standard system for old phantoms in leg phantom	36
Table 2-17	Normalized, geometrical and overall MDL ratios for bare phantoms	37
Table 2-18	Normalized, geometrical and overall MDL ratios for the old phantoms in leg phantom	37
Table 2-19	MDL ratios of cloverleaf system and modified standard system for the Monte Carlo simulations of the bare bone and the measurements of the bare phantom (a)	38
Table 2-20	MDL ratios of cloverleaf system and modified standard system for the Monte Carlo simulations of the bare bone in soft tissue and the measurements of the bare phantoms in leg phantom (a)	38
Table 2-21	MDL ratios of cloverleaf system and modified standard system for the Monte Carlo simulations of the bare bone and the measurements of the bare phantom (b)	38
Table 2-22	MDL ratios of cloverleaf system and modified standard system for the Monte Carlo simulations of the bare bone in soft tissue and the measurements of the bare phantoms in leg phantom (b)	38
Table 3-1	System setup parameters	56
Table 3-2	Ca/Coh and S/Ca ratios for the new phantoms and old phantoms	59
Table 3-3	Sample information and measurement result for NAA	60
Table 3-4	Nuclear factors for the NAA of S and Ca element	61
Table 3-5	Element concentrations of new phantoms obtained from chemical analysis	63
Table 3-6	The resolutions and their corresponding Ca edge/Coh peak ratios	65
Table 3-7	The resolutions and their corresponding Ca edge/Coh*FWHM ratios	67
Table 3-8	Ratios of beta/coh, alpha/coh and beta/alpha for the three positions of the bare bone	69
Table 3-9	Average ratios of beta/coh, alpha/coh, and beta/alpha at three bone positions of the bare bone	69

The improvement of in vivo xrf lead measurement system

Chapter1 Introduction

1.1 History of lead

Lead is a soft, blue-gray, naturally occurring heavy metal. In nature it is segregated, chiefly existing in insoluble and biologically inoffensive forms in the environment. However, human beings have disinterred it and, in doing so, released large quantities into the air, soils and surface waters.

The earliest known use of lead occurred at least five thousand years ago, for which the lead was used as an artistic material. In the days of the Egyptian Pharaohs lead was used to glaze pottery, to make solder, and to make ornamental objects. The Babylonians used soldered lead sheet for the flooring of gardens, for caulking, and to fasten into masonry. The Assyrians used to fasten bolts into masonry by pouring the lead around the bolt in the hole. Ancient China, Greece, Rome and India also have records of using lead as coins, cosmetics, pipes, pigments and even the additive to beverages *[1].

In 1926, tetraethyl lead (TEL) was introduced as an antiknock additive in gasoline to increase gasoline octane and counter engine “knock”. Since then, the burning of gasoline has been the largest source of lead in the atmosphere. The improvement of industry in 20th century also led to an increasing release of the lead to the environment, which includes emissions from iron and steel production, smelting operations, municipal waste incinerators and lead-acid-battery manufacturers *[2]. Now, lead and its compounds can be found in all parts of environment with a substantial concentration. From the estimation by both theoretical extrapolation and the measurement of lead in remote parts of the earth

*: Extracted from the website; the address of the website is listed in the reference.

and in the remains of ancient man, researchers concluded that the natural lead concentration in air to be some 3-5 orders of magnitude less than current levels, at about 0.0005micro g/m³, and in water, 2-3 orders of magnitude less, at about 0.5micro g/l *[3]. Due to its widespread use and vast distribution, lead has been considered to pose a greater health and environmental hazard than any other element. The toxic properties of lead have been recognized for over two centuries, while serious concern about it has occurred only in recent decades.

1.2 the effects of lead on human health

1.2.1 Neurological effects

That lead is potentially toxic to the nervous system has been recognized for nearly 200 years. Among occupationally exposed adults, neurological symptoms such as optical atrophy, tremors and wrist drop were recognized as the consequence of excessive lead absorption by the turn of the century (Ratcliffe J M, 1981). Lead can affect both the central nervous system and the peripheral nerves. Encephalopathy is the most severe form of lead poisoning, and is most frequently seen today in young children. It can cause dullness, restlessness, irritability, headaches, muscular tremor, hallucinations, and loss of memory and ability to concentrate. The brain lesions in fatal cases of lead poisoning are cerebral oedema and changes in cerebral blood vessels. Neurological sequelae can occur in severe or repeated episodes of lead encephalopathy. A major concern today is that young children with elevated lead exposure may be experiencing subtle neurological damage without ever exhibiting classical signs of lead encephalopathy (Environmental

Health Criteria 3, 1977). This damage may lead to deficits in neurological development; lower IQ, reading disabilities and so on.

1.2.2 Haematologic effects

Lead inhibits the body's ability to make haemoglobin by interfering with several enzymatic steps in the haem synthesis pathway. Lead inhibits at least two enzymes. The first, δ -aminolaevulinic acid dehydratase (ALAD) is the sulphhydryl enzyme responsible for the condensation of two molecules of δ -aminolaevulinic acid (ALA) to form one molecule of porphobilinogen (PBG) which has been shown to be inhibited by lead. Inhibition of this enzyme occurs in the erythropoietic tissue of the bone marrow, in circulating erythrocytes, and in the liver, kidney, and brain. Also, lead interferes with the insertion of Fe^{3+} into protoporphyrin IX, the final, intra-mitochondrial step in the synthesis of haem either by inhibition of haem synthetase (ferrochelatase) which catalyses this step, and/or by interference with the prior transport of Fe from the cytoplasm into the mitochondria. Lead also causes anaemia by shortening of the life-span of the erythrocyte. The possible mechanisms include increased osmotic resistance and increased mechanical fragility (Ratcliffe J M, 1981).

1.2.3 Renal effects

A direct effect on the kidney of long-term lead exposure is nephropathy. Impairment of proximal tubular function manifests in aminoaciduria, glycosuria, and hyperphosphaturia. Gout may develop as a result of lead-induced hyperuricaemia, with selective decreases in the fractional excretion of uric acid before a decline in creatinine clearance. There's also

evidence of an association between lead exposure and hypertension, an effect that may be mediated through renal mechanisms (Ratcliffe J M, 1981).

1.2.4 Reproductive and developmental effects

Increasing evidence indicates that lead not only affects the viability of the fetus, but development as well. An increased frequency of miscarriages and stillbirths among women working in the lead trades was reported. Developmental consequences of prenatal exposure to low levels of lead include reduced birth weight and premature birth. Chronic exposure to lead also affects the male reproductive system by reducing sperm counts and motility (Ratcliffe J M, 1981).

1.3 Lead metabolism in human body

There are two main ways for the lead to be transferred to human body. It can be inhaled into the lung by respiration, from which, 35-40% would be deposited in the lung. The lead deposited in the lung would be transferred to the GI system and blood in the proportion of 5% and 95% respectively. It can also be ingested by mouth and then transferred to the GI system. The lead transferred to the GI system would go to the blood through the small intestine. So the blood lead is an important index for short-term lead exposure. Since the lead is a bone-volume-seeking element, a substantial proportion (40%-50%) of lead in blood would be transferred to bone within a few months after exposure. Because lead remains in bone much longer than in other tissues, some 95% of total lead in an adult's body is stored in bone. The lead can also be transferred to the

brain, kidneys, liver, other soft tissues, hair and skin (Leggett R W, 1993). Another way for lead to be transferred to human body is through skin *[4].

1.4 X-ray Fluorescence (XRF)

1.4.1 Interactions of photons with specimen

When a monochromatic beam of x-ray photons falls onto a given specimen, four basic phenomena may result.

a) Photoelectric absorption

In the photoelectric absorption process, a photon undergoes an interaction with an absorber atom in which the photon completely disappears and an energetic photoelectron is ejected by the atom from one of its bound shells. For photons of sufficient energy, the most probable origin of the photoelectron is the most tightly bound or K shell of the atom. The photoelectron appears with an energy E_e given by

$$E_e = h\nu - E_b \dots\dots\dots (1-1)$$

Where E_b represents the binding energy of the photoelectron in its original shell and $h\nu$ is the energy of the incident photon. In addition to the photoelectron, the interaction also creates an ionized absorber atom with a vacancy in one of its bound shells. This vacancy is quickly filled through rearrangement of electrons from other shells of the atom and eventually capture of a free electron from the medium. Therefore, one or more characteristic x-ray photons may also be generated. In some fraction of the cases, the emission of an Auger electron may substitute for the characteristic x-ray in carrying away the atomic excitation energy. The characteristic x-ray ejected while the electron jumps from L shell to the vacancy of K shell is called

K_{α} x-ray. The energy of the x-ray equals to the difference of the binding energies of these two shells, i.e. $E_{K\alpha}=E_{bK}-E_{bL}$, where E_{bK} and E_{bL} represent the binding energies of K shell and L shell. The electron can also jump to the vacancy of K shell from M shell and the x-ray ejected is called K_{β} x-ray. Similar situation occurs for the L, M, ...electron shells for which the characteristic x-rays are called L_{α} , L_{β} , M_{α} , M_{β} , ... x-rays. Since the x-ray energy is determined by the binding energies of atomic electron shells, which are in turn determined by the charge on the atomic number, we can determine the type and concentration of the element by measuring the energy and activity of the characteristic x-rays. This is the principle of XRF measurement.

b) Compton scattering

The interaction process of Compton scattering takes place between the incident photon and an electron in the absorbing materials. In Compton scattering, the incoming photon is deflected through an angle θ with respect to its original direction. The photon transfers a portion of its energy to the electron, which is then known as a recoil electron. Because all angles of scattering are possible, the energy transferred to the electron can vary from zero ($\theta = 0$) to a substantial fraction of the photon energy (25.6% at $\theta = \pi$ for 88keV photons). Compton scattering offers little information for the in vivo XRF analysis of tissues, yet is often a dominant spectral feature. Geometry and source energy considerations are important in order to minimize the Compton scattering contribution in XRF analysis.

c) Pair production

If the gamma-ray energy exceeds twice of the rest-mass energy of an electron (1.02MeV), the process of pair production is energetically possible. In the interaction, the photon disappears and is replaced by an electron-positron pair. Since this phenomenon would never happen for the ¹⁰⁹Cd γ -ray induced lead x-rays, we are not going to illustrate it in detail here.

d) Coherent scattering

In addition to Compton scattering, another type of scattering can occur in which the photon interacts coherently with all the electrons of an absorber atom. The probability of coherent scattering is significant only for low photon energies and is most prominent in high-Z materials and at small angles with respect to the incident photon direction. The expression of the probability of coherent scattering is shown below:

$$d\sigma = \frac{1}{2} r^2 (1 + \cos^2 \theta) |F(K)|^2 d\Omega \dots\dots\dots (1-2)$$

where r is the classical electron radius, θ is the angle of scatter, and F(K) is the atomic form factor, which is a function of atomic number, Z, photon energy, E, and θ . At very small angles the cross section varies as Z^2 and this dependence on atomic number increases at large scattering angles (120°-180°), for which the cross section varies by Z^5 or Z^6 . For this reason the major source of coherently scattered photons at large scattering angles are high Z elements. This is a very important factor in the normalization procedure for determining lead concentration in the bone.

1.4.2 In vivo x-ray fluorescence measurement of lead in bone

In 1976, Ahlgren et al reported the first in vivo measurements of bone lead in human bodies by using XRF, where gamma rays from ^{57}Co were used to excite the K series x-rays of lead in finger bone with a 90-degree geometry (Ahlgren L. et al., 1976). However, the use of ^{109}Cd was soon found to have significant advantages (Todd A C, Chettle D R, 1994).

The lead detection system used in the Medical Physics group at McMaster University is a ^{109}Cd source induced KXRF system (Gordon C L et al., 1993). The ^{109}Cd source emits gamma rays of 88.035 keV in 3.6% of its decays. The energy of these gamma rays is just above the energy threshold for the K shell absorption edge in lead (88.002) and thus maximizes the photoelectric cross section and hence the x-ray fluorescence yield per incident photon. The gamma rays can interact with a K shell electron in lead and eject it. There would be a vacancy in the K shell and the electrons from L shell and M shell can jump up and fill it. The energy would be released as K_{α} or K_{β} x-rays (96% of transitions) or Auger electrons.

The energy of the lead K x-rays are listed below:

$$K_{\alpha 1} = 74.969\text{keV}$$

$$K_{\alpha 2} = 72.804\text{keV}$$

$$K_{\beta 1} = 84.936\text{keV}$$

$$K_{\beta 3} = 84.450\text{keV}$$

$$K_{\beta 2} = 87.300\text{keV}$$

The relative intensities of the x-rays are 49.19%, 29.17%, 10.92%, 5.7% and 5.02% for $K_{\alpha 1}$, $K_{\alpha 2}$, $K_{\beta 1}$, $K_{\beta 3}$ and $K_{\beta 2}$ respectively. The $K_{\alpha 1}$ and $K_{\alpha 2}$ peaks are the most intense, but

the peaks are located closer to the main Compton feature than are the K_{β} x-rays. We know that the final energy of the Compton scattering photon is:

$$E'_{\gamma} = \frac{E_{\gamma}}{1 + \alpha(1 - \cos\theta)} \dots\dots\dots (1-3)$$

where $\alpha = E_{\gamma} / mc^2$, E_{γ} is the initial energy of the photon, θ is the angle of scatter, and mc^2 is the rest mass energy of the electron. Since the backscatter geometry of about 160 degrees is used, the Compton scattered photons have a peak at energy 66.5keV. In practice, this peak exhibits Doppler broadening due to the momentum distribution of bound electrons involved in Compton scattering. The Doppler broadening of the Compton scattering gives rise to a big background for the $K_{\alpha 1}$ and $K_{\alpha 2}$ peaks, which greatly affects the precision with which these two peaks can be analyzed. For the peaks of $K_{\beta 1}$ and $K_{\beta 3}$, although the intensity is relatively small, their background is much smaller than that of the $K_{\alpha 1}$ and $K_{\alpha 2}$ peaks. So both K_{α} peaks and K_{β} peaks have their own advantage and disadvantage. In practice, we measure the lead concentration using both series of peaks. The ways for the fitting of K_{α} peaks and K_{β} peaks would be illustrated in detail in Chapter 3.

Figure 1-1 shows a spectrum of xrf lead measurement of a phantom with a lead concentration of 200ppm. It's part of the whole spectrum which includes the K_{α} peaks, K_{β} peaks and coherent peak.

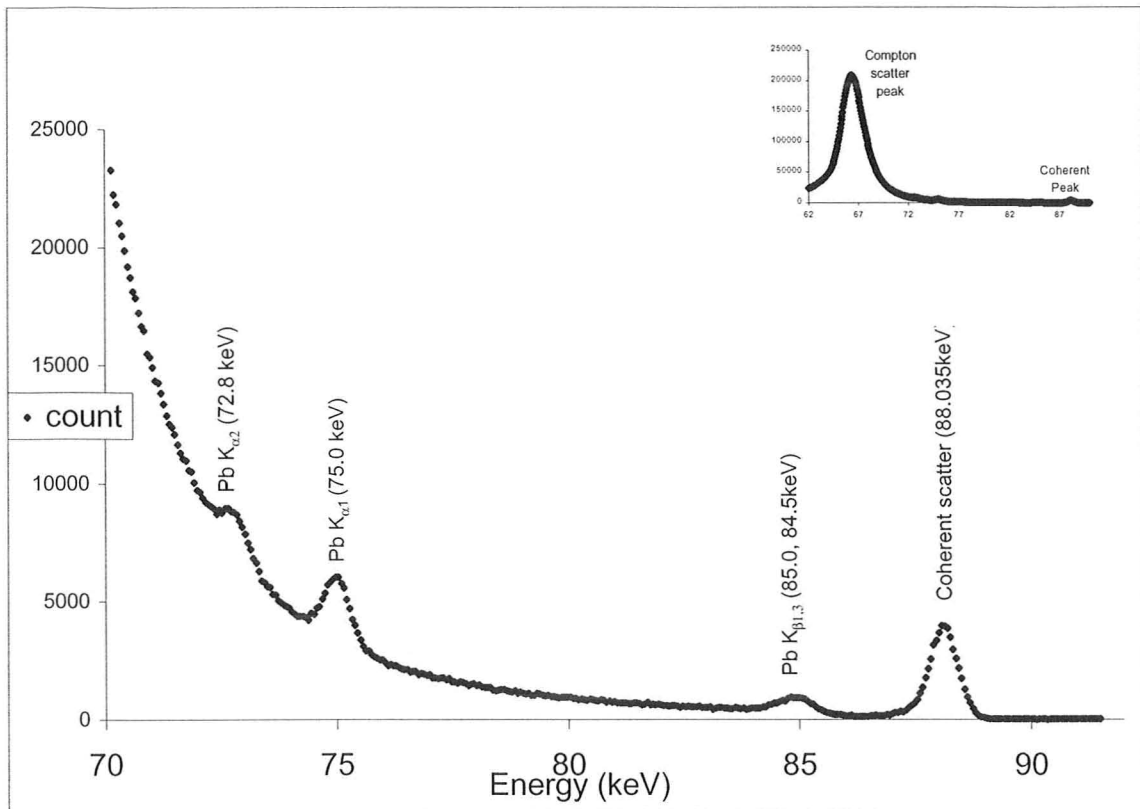


Figure 1-1 the lead xrf spectrum

1.5 In vivo xrf lead measurement system used in the project

The lead measurement system used for this project consists of a high purity germanium (HPGe) detector, a fast spectroscopy amplifier, an analog-to-digital converter (ADC), and a multichannel analyzer (MCA). The radius of the detector is 25mm and the active area is about 2000mm². The detector is covered by a 0.5 mm beryllium window and requires a bias high voltage of -2500 V dc. The best resolution for this system is about 550ev for 88.035keV gamma rays. Another 12mm detector was also used for the project, which will be described in detail in Chapter 2.

The ¹⁰⁹Cd source is positioned in a tungsten collimator at the center of the detector face, so that the 88.035keV photons can't enter the detector at 180 degrees and the scattering

angle is about 160 degree. The ^{137}Cs source is placed in a stainless steel capsule and the collimator of the source was fitted with a 0.5 mm thick copper filter to absorb the Ag K x-rays associated with the decay of ^{137}Cs . During the measurement, the sample would be fixed at about 10-30mm away from the source. The dead time for the phantom measurement is about 10% and the dead time for the in vivo measurement is usually controlled below 40%.

1.6 Brief introduction of the thesis

In this thesis, two pieces of work based on the in vivo lead measurement system will be described in detail. One is a study of MDL improvement for the lead measurement system and the other is an investigation about the lead measurement calibration. In the first work, a cloverleaf system consisting of four small detectors was used to improve the MDL for the in vivo lead measurement in bone and the comparison with the conventional system in different geometries will be discussed. In the second work, two sets of phantoms (both supposedly plaster of Paris) were measured and the calibration lines were obtained. Since there's a significant difference between the two calibration lines for fitting the lead K_{β_1, β_3} x-rays, the concentrations of certain elements in these two sets of phantoms were investigated by a modified spectrum fitting program as well as some other analysis methods, which indicated that the composition of one set of phantoms was not the same as that of the other set of phantoms. The effect of detector resolution on calibration will also be discussed in the second work.

2.1 Introduction

As mentioned above, the first in vivo measurements of bone lead in human bodies by using XRF was reported in 1976 by Ahlgren et al. (Ahlgren L. et al. 1976), where gamma rays from ^{57}Co were used to excite the K series X-rays of lead in finger bone with a 90-degree geometry. After that, a number of XRF systems have been designed and constructed for the in vivo measurement of lead concentrations in bone. According to Todd A C and Chettle D R's review in 1994, the majority of these studies adopted the ^{109}Cd K XRF method because of its several advantages: a robust measurement, a lower detection limit, and a lower effective radiation dose (Todd A C and Chettle D R, 1994).

Although the ^{109}Cd K XRF method has been considered as an effective method, the capacity of this system is not good enough to satisfy the low-level lead concentration investigations. Generally, the average bone lead concentration for non-occupationally exposed adults is about 2-3 micro g Pb/(g bone mineral) (McNeill F E et al. 1999, Hoppin J A et al. 1995) and the value maybe even lower for children, while the minimum detectable limit (MDL) for a standard system (the optimal set-up for our conventional ^{109}Cd K XRF bone-lead measurement system) is about 9 micro g Pb/(g bone mineral) (Chettle D R et al. 1991, Hoppin J A et al. 1997). So the bone lead concentration for the general population is much lower than the MDL, which means we would get a poor result for the bone-lead measurement for the general population. Since the hazardous effects at low levels of lead for the general population especially for children have been increasingly of concern, the improvement of MDL and hence the improvement of this system is becoming an important aspect for bone-lead measurement.

In recent years, some studies about the improvement of the ^{109}Cd K XRF measurement system have been reported. Ao Q et al. investigated the possible design optimizations by a specific purpose Monte Carlo code CEARXRF (Ao Q et al., 1997a, Ao Q et al., 1997b). Bateman SN et al. did some research in the improvement of the digital spectroscopy system (Bateman S N et al., 2000). Monte Carlo simulation has been widely used in the above investigations (Todd A C et al. 1991, Borjesson J et al. 1993, Ao Q et al. 1997a, Ao Q et al. 1997b). Compared to the conventional experimental method, Monte Carlo simulation has a lot of advantages: easy, economic and flexible. In this work, both Monte Carlo simulations and practical experiments are used to investigate a cloverleaf system, which consists of four 8mm detectors instead of the conventional one 25mm detector. The advantage of a small detector is that it has a better resolution and each of the four smaller detectors can process the same number of counts per unit time as the larger detector. This leads to a much better MDL by using a stronger source.

2.2 System setup

2.2.1 Standard system:

For the convenience of understanding, the standard system in this paper refers to the optimal conventional system (Gordon C L et al., 1993). The standard system consists of a 25 mm radius HpGe detector (the resolution is about 750ev for 88.035keV peak with a shaping time of 1 μs), a preamplifier, a main amplifier, an analog-to-digital converter and a PC based multi-channel analyzer system. The connection of the system is plotted in figure 2-1.

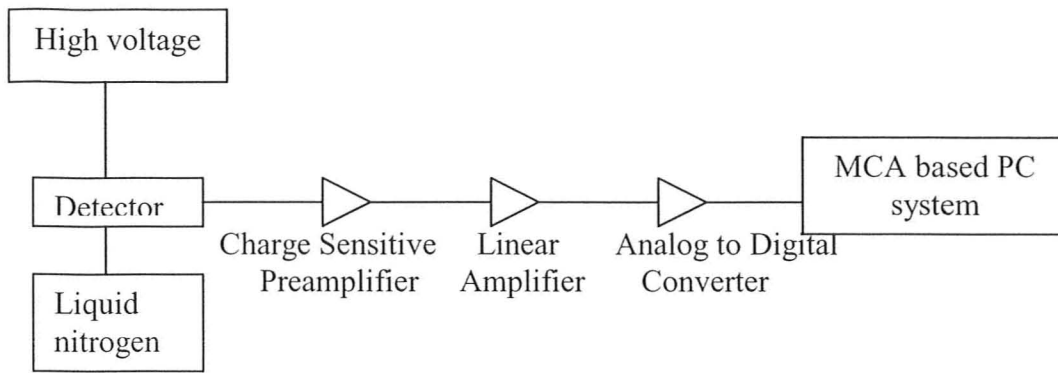


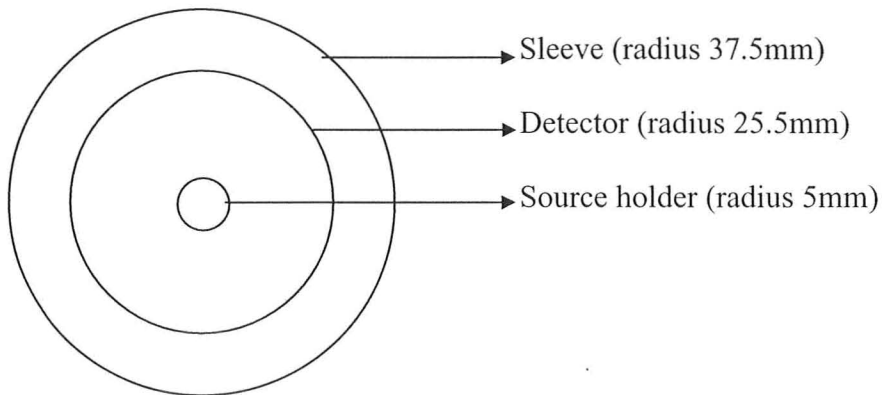
Figure 2-1 the detector system setup

2.2.2 Cloverleaf system:

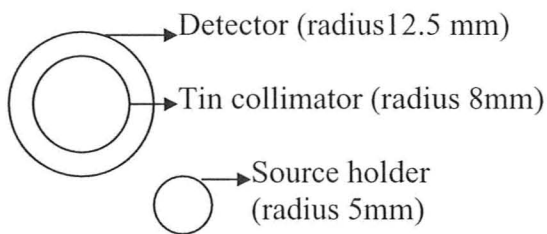
The cloverleaf system has the same electronic constituents as the standard system and the only difference is that its detector system consists of four 8mm radius small detectors and therefore four sets of the same electronic systems are needed. We had only one 12.5mm radius detector in hand and Canberra Industries loaned the 12.5 mm radius detector for a limited period of time. In this experiment, we used this detector and one set of electronics to simulate the four detector system. We covered the 12.5 mm detector by a tin collimator to simulate the 8 mm detector. The results for the 12.5 mm and 8 mm detector are both obtained for comparison.

Since the main difference for these two systems is the set-up of the detectors, this set-up will be mainly illustrated here. The facade of the detector for the standard system and the cloverleaf system is plotted in figure 2-2. Note that in the conventional system, the source is mounted in the middle of the big detector while in the cloverleaf system the source is mounted in the middle of the whole four small detectors. The plot for the cloverleaf system simulated by one small detector is also illustrated. There are two conditions for the spacing (the distance from the center of one detector to the center of the other neighboring detectors) between the four detectors in the cloverleaf system. If the cryostat

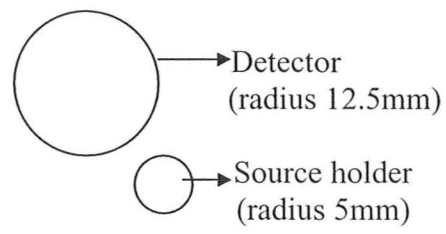
(a vacuum tight container) were mounted between the detectors, then the spacing would be 13 mm; otherwise the spacing would be 2mm. The results for these two conditions were both obtained and compared.



a) Cross-section of the standard system

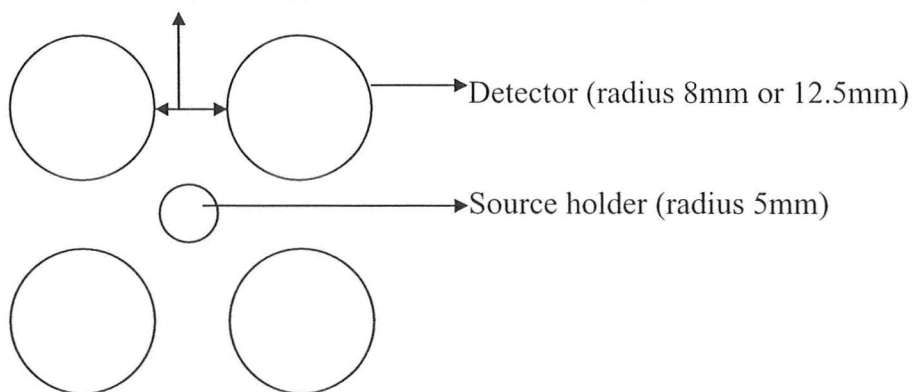


b) Cross section of the cloverleaf system with only one 8mm radius detector



c) Cross section of the cloverleaf system with only one 12.5mm radius detector

Space between two neighboring detectors (2mm or 13mm)



d) cross-section of cloverleaf system with four 8mm radius detectors

Figure 2-2 the horizontal cross-section of the cloverleaf detectors

Figure 2-2 illustrates the geometry of the detectors in horizontal cross section. The following is the illustration for the vertical geometry of the detectors. The distance from the source to the face of the detector for standard system consists of 4 parts: the detector-window distance (5mm), the source holder length (6mm), the tungsten backing on source holder (2mm) and the plastic cover of sleeve (1mm). So the minimum detector-source distance for standard system is about 14mm. For the cloverleaf system, there's an extra part: the tin collimator (for 8mm detector) which is about 2mm thick. So the minimum detector-source distance for cloverleaf system is about 16mm. A vertical cross section of the geometry for the standard system is illustrated in figure 2-3 (we can get the geometry for the cloverleaf system by adding 2 mm tin collimator thickness).

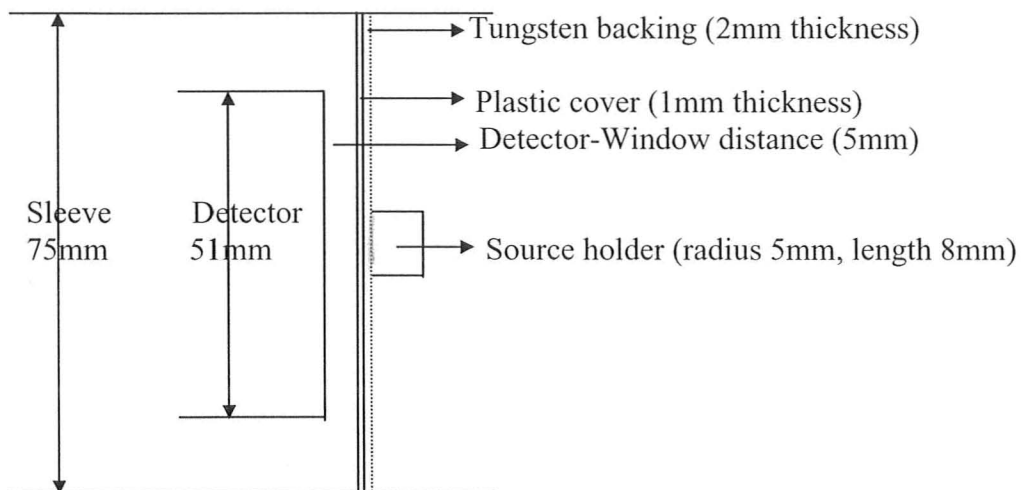


Figure 2-3 the geometry of the standard system

For the convenience of comparison, another set-up has been used. It is similar to the standard system except not subtracting 2 mm tin collimator thickness so that the minimum detector-source distance for this system is the same as the cloverleaf system (16mm). We call this system as a modified standard system in this paper. Also, for the standard system, the source-sample distance is fixed which is always 24 mm and gives

rise to a detector-sample distance of 38mm. While for the modified standard system and the cloverleaf system, we can change the source sample distance as well as the source detector distance to compare the results for different geometries. Two sets of phantoms have been used in this work. One set was made recently and we called it new phantoms. The other set was used for several years and we called it old phantoms. The radius of the new phantoms and the old phantoms are 25mm and 12mm respectively. The heights of these two sets of phantoms are 100mm. For the new phantoms, we measured it directly, so they were also called bare phantoms. For the old phantoms, we insert them into a big soft tissue phantom to simulate the in vivo measurement, so they were also called the old phantoms in leg phantom. The geometry for the old phantoms in leg phantom is illustrated in figure 2-4. The upper figure is a vertical section and the lower figure is a horizontal section.

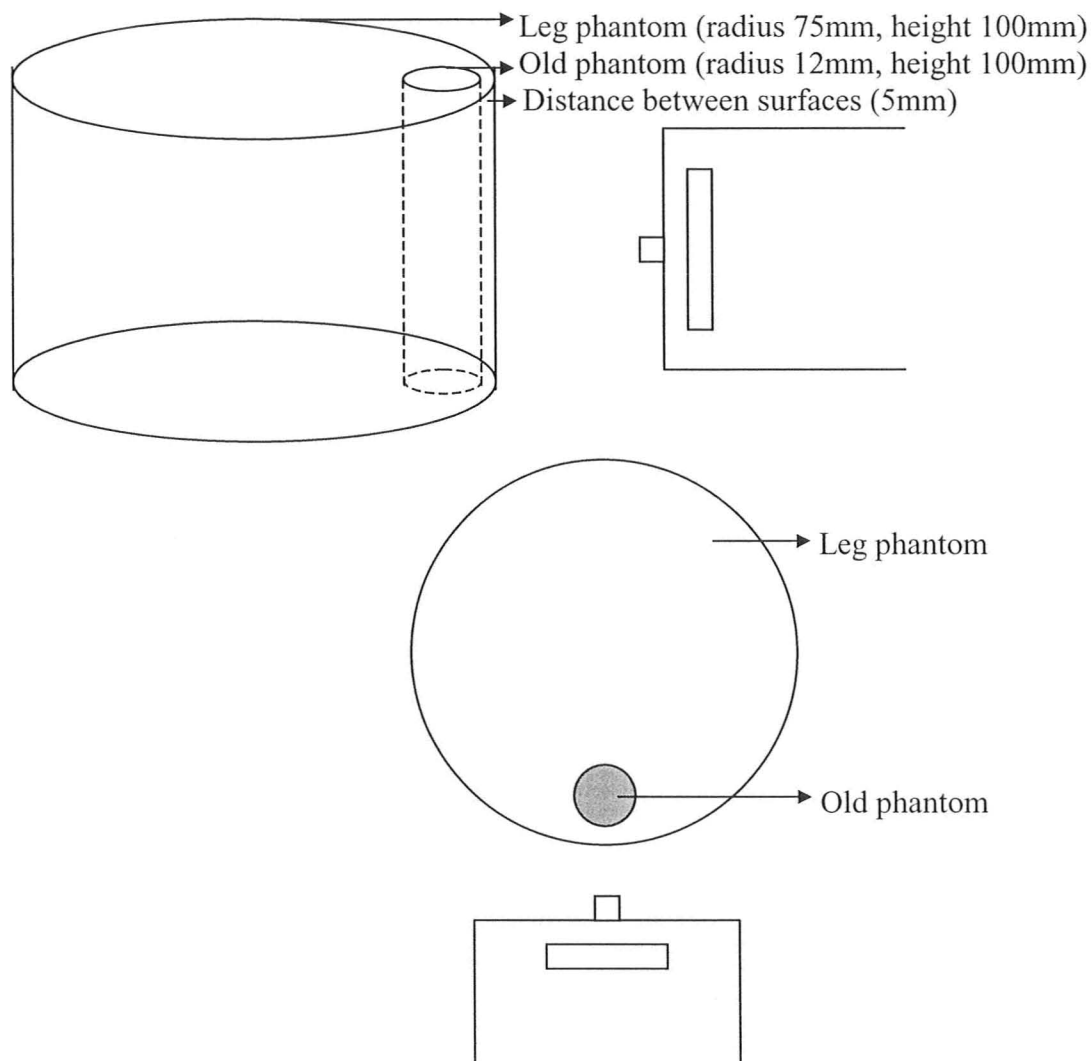


Figure 2-4 geometry of old phantom in leg phantom

2.3 Monte Carlo simulation

A Monte Carlo simulation program simulated the similar procedures experienced by the measurement of these two sets of the phantoms. This program was developed by J M O'Meara and I M Stronach and it was used in several studies before (O'Meara J M et al., 1998, 2000, Stronach I M et al., 2000). In the simulation, the old phantom in leg phantom was replaced by bone in soft tissue, which is more close to the in vivo measurement. A system comprising four small 8mm radius detectors was used instead of one collimated

8mm detector in the measurement described above. The performance of the 25mm detector was also simulated.

By operating the program, the user can specify the depth and size of the bone by an input data text file. For the bone in soft tissue simulation, we used the same depth and size as the old phantom in leg phantom used in the measurement, which has been illustrated in figure 2-4. This input file also allows the user to set the distances from the sample to the source and the detector and the concentration of the lead. The cross sections of the interactions which are expected in this simulation are also listed in the input files. So the interactions that would be created and/or detected can be determined by these parameters and hence be traced and counted by the program. The information we need for the calculation of the MDL would go to the result file.

2.3.1 Principle

The γ -rays are generated with random direction from the source. The geometry of the system is used to determine whether or not the γ -ray hits the sample. If the photon misses, the event is terminated, recorded as a miss, and the next γ -ray is generated. For γ -rays that hit the sample surface, the distance to the first interaction is calculated based on the relevant attenuation cross-section(s), accounting for the different media encountered along the path of the photon. If the corresponding site for this interaction is within the sample, the particular interaction is selected using a random number and the relevant photoelectric, Compton and coherent cross sections of either soft tissue or bone. For the photoelectric events, the cross section for different kinds of characteristic x-rays are used

and the yields for different kind of x-rays are obtained. The yield of the coherent scattering also can be obtained. Both of the results are needed for the calculation of the MDL. They are written to the output files.

2.3.2 MDL calculation for the MC simulation

If the measurement value for a sample obeyed Gaussian distribution A, we can say with 95% confidence that the true value for the sample is $A \pm 2\sigma_A$. For the same reason, if the background counts under the lead x-ray energy in the spectrum is N, then if the total counts under the x-ray energy is bigger than $N + 2\sigma_N$, we can determine with 95% confidence that there are sufficient lead x-rays to be detected above the background. This is the principle to calculate the MDL in MC simulation. The formula for the MDL calculation for MC simulation is shown below

$$MDL_{raw} = 2 \times C \times \frac{N_{x0}}{N_{coh}} \times \sqrt{\frac{1}{N_{x0}} + \frac{1}{N_{coh}}} \dots\dots\dots (2-1)$$

where N_{x0} is the count at x-ray energy for 0ppm lead concentration, N_{coh} is the count in coherent peak and C (micro g Pb/g bone mineral) is calibration factor. C is derived from the N_x/N_{coh} versus phantom Pb concentration in micro g Pb/g bone mineral. Here

$\frac{N_{x0}}{N_{coh}} \times \sqrt{\frac{1}{N_{x0}} + \frac{1}{N_{coh}}}$ is the uncertainty of $\frac{N_{x0}}{N_{coh}}$. In the simulation, the x-rays are under a

point energy, but in the measurement, the x-ray counts are under an energy range and this range is determined by the resolution of the detection system. For this measurement, the energy range we selected for the calculation of N_{x0} is 6σ ($\pm 3\sigma$), where σ is the standard

deviation of the gaussian peak of the x-ray. Since $\sigma = \frac{FWHM}{2.355}$, 6σ

$$= 6 * \frac{FWHM}{2.355} = 6 * \frac{750ev}{2.355} \approx 2keV .$$

For the convenience of calculation, we only did the simulation of the $K_{\alpha 1}$ x-ray, whose x-ray energy is 74.969 and corresponds to a background range of 74-76keV. The above formula is for the calculation of the raw MDL. As mentioned before, one of the advantages of the small detector is its improved dead time. That is, we can use a stronger source for the small detector system to get a better signal and hence a better MDL. Since the dead time of the system is decided by the total events detected by the detector, we can normalize the MDL of the small detector system with the total detected events. The normalized MDL can be expressed as following:

$$MDL_{normalized} = MDL_{raw} \times \sqrt{\frac{N}{N_0}} \dots\dots\dots (2-2)$$

where N is the total events detected by one of the four 8mm small detectors, and N_0 is the total events detected by the corresponding 25mm detector system.

2.3.3 Monte Carlo setups

As mentioned above, a bone in soft tissue was used in the Monte Carlo simulation to simulate the in vivo samples. The position of the bone and tissue is the same as the old phantom in leg phantom as we illustrated above in the setup of the measurement. In the simulation, the origin is set at the center of the tissue phantom and the horizontal direction is set to be the y direction. The main input parameters for the two sets of phantoms are as following:

Target	Lead
Source	^{109}Cd
DSD (detector sample distance)	30mm, 25mm, 22mm, 20mm, and 38mm
SSD (source sample distance)	14mm, 9mm, 6mm, 4mm, and 24mm
Detector radius	25mm and 8mm
Tissue phantom radius	25mm and 75mm
Tissue phantom height	100mm
Bone radius	25mm and 12mm
Bone offset (from origin)	0mm and 58mm
Number of photons exit the collimator	5e8
Concentration of the target	0ppm and 200ppm
Number of detector	1 for 25mm detector and 4 for 8mm detector

Table 2-1 input parameters for the Monte-Carlo simulation

2.3.4 Monte Carlo simulation results:

i) Comparison of the Monte Carlo spectrum with the measurement spectrum.

Figure 2-5 shows the comparison of the Monte Carlo spectrum with the measurement spectrum for the 25mm radius detector and 200ppm lead concentration at the energy range 58keV to 89keV (for bone in tissue simulation and the old phantom in leg phantom measurement).

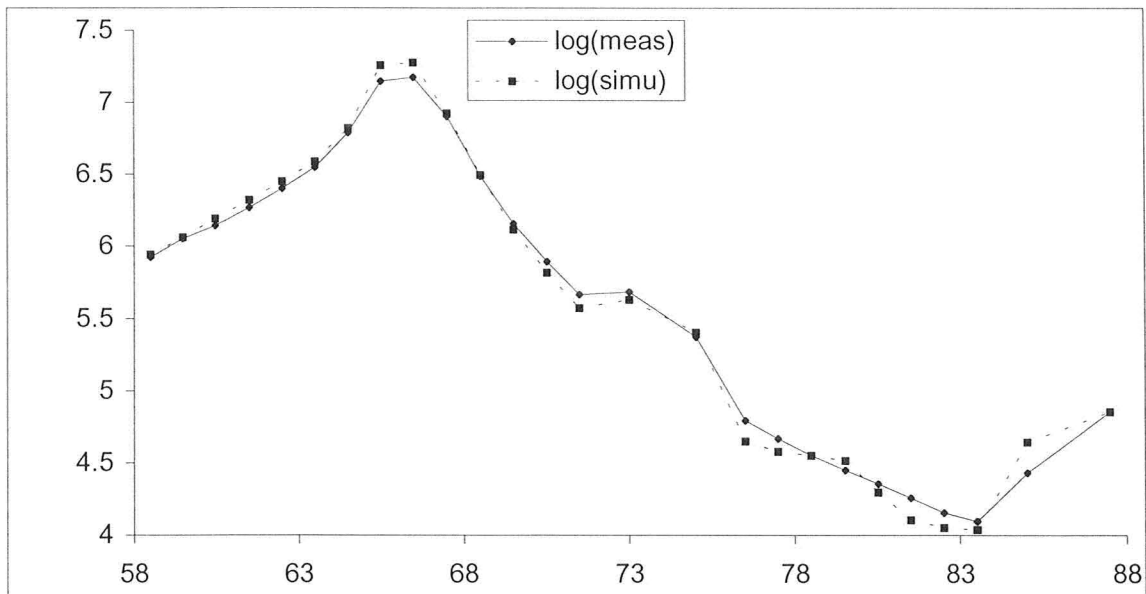


Figure 2-5 comparison of the spectrum (log scale) for Monte Carlo simulation and the Measurements at energy range 58keV to 88keV

Note: Slight differences between soft tissue as simulated and the soft tissue phantom material may account for a part of the minor systematic difference between simulated and measured spectra. Difference in coherent cross section for bone in soft tissue as simulated and the phantom in soft tissue phantom may account for minor difference of the coherent peak.

Figure 2-6 shows the comparison of the spectrum near the $K_{\alpha 1}$ peak (74.969keV) and the coherent peak.

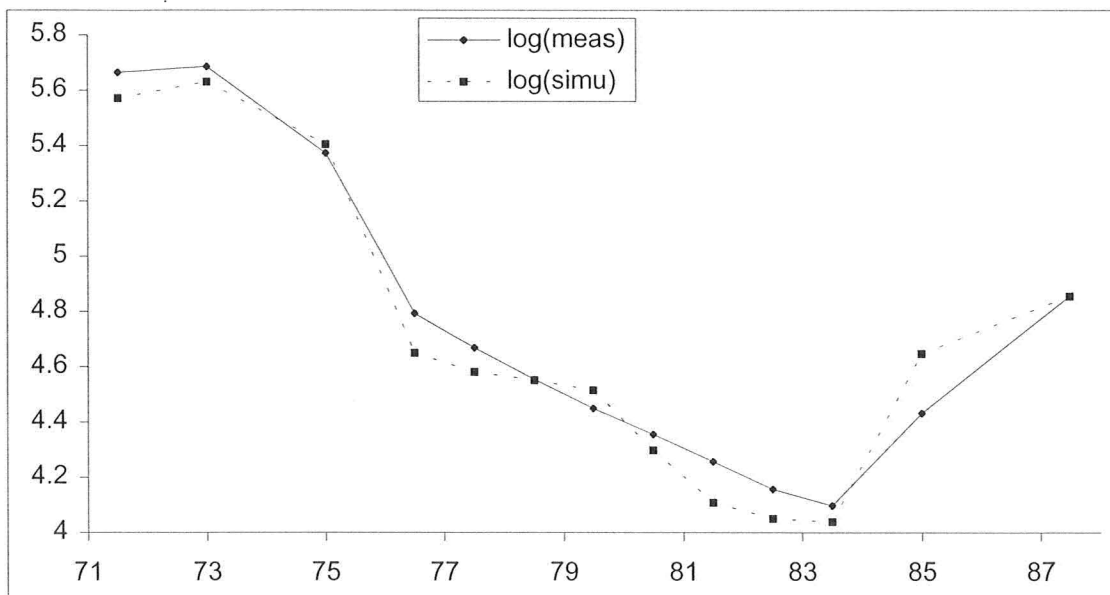


Figure 2-6 comparison of the spectrum (log scale) for Monte Carlo simulation and the measurements at energy 71keV to 88keV

Table 2-2 shows the comparison of the counts in related areas obtained from Monte Carlo simulation and measurement for the 25mm radius detector and 200ppm lead concentration.

Spectral feature	Monte Carlo	Experiment
K _{α1} x-ray area (74.0 to 76.0keV)	2.82×10 ⁵	(2.36±0.05)×10 ⁵
Coherent area	6.05×10 ⁴	(5.39±0.03)×10 ⁴
Total area from low-energy side of Compton (60.5 to 88.5keV)	6.77×10 ⁷	(5.93±0.02)×10 ⁷

Table 2-2 comparison of the counts in related areas obtained from Monte Carlo simulation and measurement for the 25mm radius detector and 200ppm lead concentration

From the above figure and table, we can see that the spectra for the Monte Carlo simulation and the measurement are quite similar. The Monte Carlo simulation exceeds the experiment consistently, by between 12.2% and 19.5%.

ii) Monte Carlo (MC) simulation MDLs

Two sets of simulation have been done. One is for the bare bone in different geometries; the other is for the bare bone in soft tissue. Table 2-3 and table 2-4 list the results for the simulation for different geometries for the modified standard and cloverleaf system as well as the standard system. Table 2-3 is the result for the simulation of the bare bone and table 2-4 is the result for the simulation of the bone in soft tissue. The MDLs were calculated by the formula illustrated above. In the table MDL25 is the MDL for the modified standard system. Modified ratio (Mod) is the raw MDL ratio of modified standard system and standard system.

geometry	raw MDLs		(not norm)		MDLstan	Modified ratio MDL25/MDLstan	Overall norm*Mod
	MDL8	MDL25	raw ratio	norm ratio			
30,14	5.532	4.042	1.369	0.465	4.698	0.860	0.400
25,9	4.939	3.779	1.307	0.451		0.804	0.363
22,6	4.663	3.702	1.260	0.439		0.788	0.346
20,4	4.552	3.714	1.226	0.431		0.791	0.340

Table 2-3 Normalized, geometrical and overall MDL ratios for bare bone by MC simulation

geometry	raw MDLs		(not norm)		MDLstan	Modified ratio MDL25/MDLstan	Overall norm*Mod
	MDL8	MDL25	raw ratio	norm ratio			
30,14	9.682	7.019	1.379	0.467	9.087	0.773	0.361
25,9	8.145	6.162	1.322	0.451		0.679	0.306
22,6	7.409	5.95	1.245	0.43		0.655	0.282
20,4	7.133	6.184	1.153	0.401		0.681	0.273

Table 2-4 Normalized, geometrical and overall MDL ratios for bone in soft tissue by MC simulation

Note: Here the scale ratios are normalized to the simulated coherent area of the modified standard system, which is corresponding to the ratios normalized to the real time coherent rates of the modified standard system.

Table 2-5 and table 2-6 show the raw MDL of standard system and the normalized MDL of the cloverleaf system for which the MDLs for the four different geometries are normalized to the simulated number of coherent counts of the standard system. Table 2-5 is the result of the simulation for the bare bone and table 2-6 is the result of the simulation for the bone in soft tissue. The ratios of these two MDLs are also listed.

Geometry	raw MDLs		(for 1 det)		norm MDL8/ MDL stan
	MDL8	MDL25	coh clover	coh stan	
30,14	5.532		3862.75		2.266
25,9	4.939		5069.75		2.318
22,6	4.663		6004.25		2.381
20,4	4.552		6721.75	23026	2.459

Table 2-5 Normalized MDL ratios for cloverleaf and standard system for bare bone by MC simulation

Geometry	raw MDLs		(for 1 det)		norm MDL8/ MDL stan
	MDL8	MDL25	coh clover	coh stan	
30,14	9.682		2100	11083	4.215
25,9	8.145		2948.75		4.202
22,6	7.409		3691		4.276
20,4	7.133		4286.75		4.436

Table 2-6 Normalized MDL ratios for cloverleaf and standard system for bone in soft tissue by MC simulation

2.4 Measurement results

2.4.1 Data analysis

(i) the calculation of MDL:

The mgerfa fitting program for lead concentration was used to get the lead concentration and the uncertainty by alpha-fitting (the fitting for the $K_{\alpha 1}$ and $K_{\alpha 2}$ peaks) and beta-fitting (the fitting for the $K_{\beta 1}$ and $K_{\beta 3}$ peaks). Please refer to Chapter 3 (3.2) for the detailed description of the fitting program. The MDL of the lead concentration using alpha-fitting and beta-fitting was calculated by the following formula:

$$(MDL)_{alpha} = 2 \times (uncertainty)_{alpha} \dots\dots\dots (2-3)$$

$$(MDL)_{beta} = 2 \times (uncertainty)_{beta} \dots\dots\dots (2-4)$$

and the weighted MDL can be estimated as (Bevington, 1969):

$$(MDL)_{weighted} = [(MDL_{alpha})^{-2} + (MDL_{beta})^{-2}]^{-1/2} \dots\dots\dots (2-5)$$

(ii) Normalization:

We can only get the results for the cloverleaf system for the given source from the fitting. To get the results for a stronger source, we need to normalize the result by coherent counts for fixed real time. The formula for the normalized MDL is as following:

$$(MDL)_{normalized} = (MDL)_{weighted} \times \sqrt{\frac{(\frac{coherent\ area}{realtime})_{clover}}{(\frac{coherent\ area}{realtime})_{standard}}} \dots\dots (2-6)$$

We don't use the real time total count rate here because the coherent count rate ratio is what we are most concerned with and the total count rate ratio is slightly different from the coherent count rate ratio due to the slight shift in spectrum for different geometries.

The ratio between the stronger source and the current source can be calculated as following:

$$(ratio)_{source} = \frac{N/t}{N_0/t_0} \dots\dots\dots (2-7)$$

where N and t are the total counts and live time for the measurement using stronger source, N₀ and t₀ are the total counts and live time for the measurement using current source.

Two kinds of samples have been used in this experiment. One is the big bare phantom (which is called new phantom in this paper) and the other is small phantom (which is called old phantom in this paper) inserted in a leg phantom, which simulates the in-vivo measurement. Three different concentrations for the two kinds of phantoms were measured respectively.

2.4.2 Measurement results:

Ten sets of setups have been used in this experiment:

- a. Using 3 iron cylinders (100 mm diameter, 28 mm height and 1.65kg for each) represent the three additional detectors to detect the effect of scattering, new phantoms;
- b. 12.5 mm radius detector cloverleaf system for 13 mm spacing with different detector sample and source sample distance (DSD and SSD) geometries, new phantoms;

- c. 8 mm radius detector cloverleaf system for 13 mm spacing with different DSD and SSD geometries, new phantoms;
- d. 12.5 mm radius detector cloverleaf system for 2 mm spacing with different DSD and SSD geometries, new phantoms;
- e. 8 mm radius detector cloverleaf system for 2 mm spacing with different DSD and SSD geometries, new phantoms;
- f. 8 mm radius detector cloverleaf system for 2 mm spacing with different DSD and SSD geometries, old phantoms in leg phantoms;
- g. Modified standard system with different DSD and SSD geometries, new phantoms;
- h. Modified standard system with different DSD and SSD geometries, old phantom in leg phantoms;
- i. Standard system with fixed DSD and SSD geometries, new phantoms;
- j. Standard system with fixed DSD and SSD geometries, old phantoms

2.4.2.1 the effect of scattering, spacing and detector radius

(i) The effect of scattering

Since we used one small detector instead of four detectors, the scattering effect of three other detectors needs to be considered. In this work, we put three Fe cylinders at the corresponding places to simulate the other three detectors and compared the results with those without the Fe cylinders. We did this for three settings:

- a. For 8 mm detector, 2 mm spacing, 30 mm detector-sample distance, 9 mm source-sample distance, the ratio of the weighted MDL obtained with Fe cylinders and without Fe cylinders is 1.009 ± 0.008 ;
- b. For 12.5 mm detector, 2 mm spacing, 30 mm detector-sample distance, 4 mm source-sample distance, the ratio of the weighted MDL obtained with Fe cylinders and without Fe cylinders is 0.960 ± 0.006 ;
- c. For 12.5 mm detector, 13 mm spacing, 30 mm detector-sample distance, 4 mm source-sample distance, the ratio of the weighted MDL obtained with Fe cylinders and without Fe cylinders is 1.028 ± 0.011 .

The biggest difference is about 4% between the settings with and without Fe cylinders, so we neglect the scattering effect in this work.

(ii) The effect of spacing

As mentioned above, the spacing between the detectors could be 2 mm or 13 mm. The ratios of the weighted MDL for these two conditions are listed in table 2-7 (The ratio here refers to the ratio of the MDL for 2 mm spacing to the MDL for 13 mm spacing).

Radius of the detector	DS distance	SS distance	Ratio
8 mm	30 mm	14 mm	0.887 ± 0.021
	30 mm	9 mm	0.819 ± 0.024
	30 mm	4 mm	0.707 ± 0.022
12.5 mm	30 mm	14 mm	0.972 ± 0.025
	30 mm	9 mm	0.977 ± 0.015
	30 mm	4 mm	0.957 ± 0.028

Table 2-7 ratio of MDL for 2mm and 13mm spacing for 8mm and 12.5 mm detectors
 Note: DS distance is the detector-sample distance; SS distance is the sample-source distance.

From the above table, we can see that the ratio of the weighted MDL for 2 mm spacing to the weighted MDL for 13 mm spacing is consistently less than 1 and that the ratio is smallest for the 8 mm radius detector with the smallest source sample distance. This means using the 2 mm spacing would give a better MDL. Although, if the 12.5 mm radius detector were used, the difference would be small.

(iii) The effect of the detector radius

From the Monte Carlo simulation, we concluded that 8 mm radius detector is the optimal choice. In this section, we'll compare the ratios of the normalized MDL for 8 mm radius detector to the weighted MDL for 12.5 mm radius detector for different DSD and SSD geometries. The results are listed in table 2-8.

Spacing of the detectors	DS distance	SS distance	Ratio
2 mm	30 mm	14 mm	0.953±0.015
	30 mm	9 mm	0.967±0.011
	30 mm	4 mm	0.955±0.009
13 mm	30 mm	14 mm	0.950±0.008
	30 mm	9 mm	0.962±0.001
	30 mm	4 mm	0.992±0.036

Table 2-8. ratio of MDL for 8mm and 12.5mm radius detectors with 2mm and 13mm spacing

From table 2-8, we can see that if we use a stronger source for the 8 mm radius detector (which leads to the similar dead time for these two detectors), the MDL for 8 mm radius detector would be better than the MDL for 12.5 mm radius detector although the advantage is not very great, all the ratios being between 0.95 and 1.00.

2.4.2.2 the comparison of the measurement results

(i) Compare the cloverleaf system with the modified standard system for the new bare phantom measurement

From the above discussion, we know that the optimal setting for cloverleaf system is 8 mm radius detectors with 2 mm spacing. So for the following sections, the cloverleaf system refers to the system with 8 mm radius detector and 2 mm spacing between the detectors. In this part, the MDLs for a given source (the ^{109}Cd source we are using now) and the normalized MDLs are compared respectively. Also, in this work, we measured the phantoms with three different concentrations for both new phantoms and old phantoms. So the MDL is the average of the three corresponding MDLs and the uncertainty of the MDL is the standard deviation of the three MDLs.

a. Comparison of the MDLs for a given source

Since the samples are measured for different time periods, the MDLs are adjusted to the same real time duration 1800s. So

$$MDL_{adjtime} = MDL \times \sqrt{\frac{real\ time}{1800}} \dots\dots\dots (2-8)$$

for both 8mm and 25mm detectors.

The MDL for cloverleaf and modified standard system and their ratios are listed in Table 2-9.

DS	SS	(MDL) _{clover}	(MDL) _{modified stan.}	ratio
30 mm	14 mm	2.239±0.464	2.112±0.308	1.054±0.074
30 mm	9 mm	2.223±0.445	2.144±0.348	1.033±0.039
30 mm	4 mm	2.344±0.442	2.348±0.373	0.995±0.029
25 mm	9 mm	2.003±0.413	1.949±0.320	1.023±0.042
22 mm	6 mm	1.913±0.341	1.903±0.265	1.002±0.037
20 mm	4 mm	1.875±0.323	1.893±0.252	0.987±0.041

Table 2-9 MDL ratios for cloverleaf and modified standard system for new bare phantoms

Note: the unit for the MDL is micro g/(g bone mineral).

So, if we don't change the source, the MDL for the cloverleaf system is only a little bit better than the MDL for the modified standard system and only when the source sample distance is small. Since the dead time for the cloverleaf system for a given source is below 4% while the dead time for the modified standard system is about 20%-40%, it's feasible for us to increase the source strength for the cloverleaf system 5 to 10 times for different geometries.

b. Comparison of normalized MDLs (MDLs of cloverleaf system for a stronger source)

In this section, we normalized the MDL for the cloverleaf system by the coherent area count rate. The normalized MDL for cloverleaf system is:

$$(MDL_{clover})_{normalized} = (MDL_{clover})_{weighted} \times \sqrt{\frac{(\frac{coherent\ area}{realtime})_{clover}}{(\frac{coherent\ area}{realtime})_{modified\ standard}}}$$

here $(MDL_{clover})_{weighted}$ is the MDL that has been adjusted to the same real time.

The results listed in Table 2-10.

DS	SS	(MDL) _{clover}	(MDL) _{modified stan.}	ratio	(ratio) _{strength}
30 mm	14 mm	0.896±0.168	2.112±0.308	0.423±0.017	6.285±0.497
30 mm	9 mm	0.918±0.186	2.144±0.348	0.427±0.016	5.972±0.075
30 mm	4 mm	1.005±0.209	2.348±0.373	0.426±0.020	5.719±0.221
25 mm	9 mm	0.821±0.169	1.949±0.320	0.420±0.017	6.103±0.100
22 mm	6 mm	0.796±0.145	1.903±0.265	0.417±0.017	5.933±0.089
20 mm	4 mm	0.778±0.145	1.893±0.252	0.409±0.023	6.038±0.087

Table 2-10 normalized MDL ratios for cloverleaf and modified standard system for new bare phantoms

Note: the ratio of strength column refers to the increasing multiple of the source strength by normalizing the MDL for cloverleaf system, which can be expressed as equation 2-7.

So if we increase the source strength for the cloverleaf system to a degree that gives rise to the same coherent count rate as the coherent rate in the modified standard system with the corresponding geometry, the MDL for the cloverleaf system would be greatly improved.

(ii) Compare the cloverleaf system with the modified standard system for the measurement of the old phantom in the leg phantom

a. Comparison of the MDLs for a given source

The MDLs for cloverleaf and modified standard system and their ratios are listed in Table 2-11.

DS	SS	(MDL) _{clover}	(MDL) _{modified stan.}	ratio
30 mm	14mm	4.381±0.607	4.701±0.633	0.932±0.020
25 mm	9 mm	4.145±0.618	4.089±0.729	1.017±0.029
22 mm	6 mm	3.691±0.433	3.933±0.219	0.936±0.059
20 mm	4 mm	3.430±0.454	3.870±0.431	0.886±0.057

Table 2-11 MDL ratios for cloverleaf and modified standard system for old phantoms in leg phantom

The ratios are slightly lower than that for the bare phantoms, which are around 1.

b. Comparison of normalized MDLs (MDLs of cloverleaf system for a stronger source)

The results listed in Table 2-12.

DS	SS	(MDL) _{clover}	(MDL) _{modified stan.}	ratio	(ratio) _{strength}
30 mm	14 mm	2.149±0.321	4.701±0.633	0.457±0.009	5.055±0.046
25 mm	9 mm	1.850±0.375	4.089±0.729	0.451±0.010	5.034±0.120
22 mm	6 mm	1.657±0.226	3.933±0.219	0.421±0.043	5.136±0.074
20 mm	4 mm	1.640±0.224	3.870±0.431	0.423±0.015	5.522±0.109

Table 2-12 normalized MDL ratios for cloverleaf and modified standard system for old phantoms in leg phantom

The ratios are a little worse than that for the bare phantoms. There are two reasons for this. One is that since the old phantom is inserted in the leg phantom, there's an offset between the surface of the leg phantom and the surface of the old phantom, which leads to an actually bigger DS and SS distance. The other reason is that the leg phantom produces more interactions, which increases the background of the spectrum.

(iii) Compare the cloverleaf system with the standard system for bare phantom measurement

Since the standard system is the system we used in practice, a comparison of the cloverleaf system with the standard system has more practical meaning. The standard system has a fixed geometry with the DS distance and SS distance of 38 mm and 24 mm, so in this section the normalized MDL of the cloverleaf system for different geometries is normalized to the same real time coherent rate of the standard system.

a. Comparison of the MDLs for a given source

The MDL for cloverleaf and standard system and their ratios are listed in Table 2-13.

DS	SS	(MDL) _{clover}	(MDL) _{standard}	ratio
30 mm	14 mm	2.239±0.464	2.319±0.428	0.963±0.022
30 mm	9 mm	2.223±0.445		0.957±0.014
30 mm	4 mm	2.344±0.442		1.011±0.008
25 mm	9 mm	2.003±0.413		0.862±0.018
22 mm	6 mm	1.913±0.341		0.826±0.009
20 mm	4 mm	1.875±0.323		0.810±0.010

Table 2-13 MDL ratios for cloverleaf and standard system for new bare phantoms

Note: Here the DS and SS distance are for the cloverleaf system only.

b. Comparison of normalized MDLs (MDLs of cloverleaf system for a stronger source)

The results listed in Table 2-14.

DS	SS	(MDL) _{clover}	(MDL) _{standard}	ratio	(ratio) _{strength}
30 mm	14 mm	0.988±0.216	2.319±0.428	0.424±0.014	5.002±0.110
30 mm	9 mm	1.024±0.210		0.440±0.009	4.724±0.031
30 mm	4 mm	1.049±0.211		0.452±0.007	5.217±0.082
25 mm	9 mm	1.022±0.212		0.440±0.010	3.874±0.026
22 mm	6 mm	1.043±0.203		0.449±0.005	3.489±0.071
20 mm	4 mm	1.073±0.198		0.463±0.001	3.303±0.035

Table 2-14 normalized MDL ratios for cloverleaf and standard system for new bare phantoms

Note: here (MDL)_{clover} is the MDL of cloverleaf system normalized to the coherent count rate of the standard system. It's not the same as the (MDL)_{clover} in table 2-12, which is normalized to the coherent count rate of the modified standard system.

(iv) Compare the cloverleaf system with the standard system for the measurement of the old phantom in the leg phantom

a. Comparison of the MDLs for a given source

The MDL for cloverleaf and standard system and their ratios are listed in Table 2-15.

DS	SS	(MDL) _{clover}	(MDL) _{standard}	ratio
30 mm	14 mm	4.381±0.607	5.898±0.754	0.742±0.021
25 mm	9 mm	4.145±0.618		0.702±0.014
22 mm	6 mm	3.691±0.433		0.626±0.007
20 mm	4 mm	3.430±0.454		0.581±0.007

Table 2-15 MDL ratios for cloverleaf and standard system for old phantoms in leg phantom

b. Comparison of normalized MDLs (MDLs of cloverleaf system for a stronger source)

The results listed in Table 2-16.

DS	SS	(MDL) _{clover}	(MDL) _{standard}	ratio	(ratio) _{strength}
30 mm	14 mm	2.293±0.338	5.898±0.754	0.388±0.007	3.490±0.047
25 mm	9 mm	2.352±0.348		0.398±0.007	2.719±0.016
22 mm	6 mm	2.421±0.315		0.411±0.001	2.510±0.017
20 mm	4 mm	2.449±0.356		0.415±0.007	2.515±0.019

Table 2-16 normalized MDL ratios for cloverleaf and standard system for old phantoms in leg phantom

2.4.2.3 Geometry effect

The above ratio for standard system and cloverleaf system is the ratio for which the MDL of cloverleaf system is normalized to the coherent count rate of standard system, i.e. normalized to the same coherent count rate. If we consider the effect of geometry, then we'll get the ratio for standard system and cloverleaf system by two steps: First, compare the modified standard system and cloverleaf system in the same geometry for all the four geometries (30,14), (25,9), (22,6), (20,4). Then, compare the modified standard system and standard system for four different geometries. By multiplying these two ratios, we can get the ratio for standard system and cloverleaf system. Here, the ratio we got from the first step is the same as the normalized ratio we got in table 2-10 and table 2-12. But for the second step, since we only consider the effect of the geometry, we're not going to normalize the MDLs for the standard system, so the ratio is the ratio of the original MDLs of modified standard system and standard system (to say it precisely, the ratio is the ratio of the original MDLs normalized by real time 1800s). Table 2-17 and table 2-18 lists these ratios for bare phantom and for the old phantom in leg phantom respectively.

SSD	DSD	Normalized MDLclov/MDLmodstd	Geometrical MDLmodstd/MDLstd	overall MDLclover/MDLstd
30mm	14mm	0.423±0.017	0.915±0.046	0.387±0.011
25mm	9mm	0.420±0.017	0.842±0.018	0.353±0.008
22mm	6mm	0.417±0.017	0.825±0.036	0.343±0.004
20mm	4mm	0.409±0.023	0.821±0.042	0.336±0.004

Table 2-17 normalized, geometrical and overall MDL ratios for the bare phantom

SSD	DSD	Normalized MDLclov/MDLmodstd	Geometrical MDLmodstd/MDLstd	overall MDLclover/MDLstd
30mm	14mm	0.457±0.009	0.797±0.038	0.364±0.016
25mm	9mm	0.451±0.010	0.691±0.033	0.312±0.022
22mm	6mm	0.421±0.043	0.671±0.047	0.281±0.020
20mm	4mm	0.423±0.015	0.658±0.049	0.278±0.016

Table 2-18 normalized, geometrical and overall MDL ratios for the old phantom in leg phantom

2.4.2.4 Comparison of the results for the Monte Carlo simulation and the measurement

We got the ratios between the normalized MDLs of the cloverleaf system and the MDLs of the standard system by two methods. For the first method, we normalized the MDLs of the cloverleaf system directly by the real time coherent count rate of the standard system. For the second method, we got the ratios by two steps, which has been illustrated in the above section “geometry effect”. Table 2-19 and table 2-20 show the comparison the MDL ratios obtained by the Monte Carlo simulation and the measurements by using the first method. Table 2-21 and table 2-22 show the comparison of the MDL ratios obtained by the Monte Carlo simulation and the measurement by using the second method.

SSD	DSD	(ratio) _{MC}	(ratio) _{measure}
30mm	14mm	0.482	0.452±0.007
25mm	9mm	0.493	0.440±0.010
22mm	6mm	0.507	0.449±0.005
20mm	4mm	0.523	0.463±0.001

Table 2-19 MDL ratios of cloverleaf system and modified standard system for the Monte Carlo simulations of the bare bone and the measurements of the bare phantom (a)

SSD	DSD	(ratio) _{MC}	(ratio) _{measure}
30mm	14mm	0.464	0.388±0.007
25mm	9mm	0.463	0.398±0.007
22mm	6mm	0.471	0.411±0.001
20mm	4mm	0.489	0.415±0.007

Table 2-20 MDL ratios of cloverleaf system and modified standard system for the Monte Carlo simulations of the bare bone in soft tissue and the measurements of the bare phantom in leg phantom (a)

SSD	DSD	(ratio) _{MC}	(ratio) _{measure}
30mm	14mm	0.400	0.387±0.011
25mm	9mm	0.363	0.353±0.008
22mm	6mm	0.346	0.343±0.004
20mm	4mm	0.340	0.336±0.004

Table 2-21 MDL ratios of cloverleaf system and modified standard system for the Monte Carlo simulation of the bare bone and the measurement of the bare phantom (b)

SSD	DSD	(ratio) _{MC}	(ratio) _{measure}
30mm	14mm	0.361	0.364±0.016
25mm	9mm	0.306	0.312±0.022
22mm	6mm	0.282	0.281±0.020
20mm	4mm	0.273	0.278±0.016

Table 2-22 MDL ratios of cloverleaf system and modified standard system for the Monte Carlo simulations of the bare bone in soft tissue and the measurements of the bare phantom in leg phantom (b)

Note: This table is for the second method.

2.5 Discussion

Usually we tend to use a larger detector to improve the measurement system. In this work, we use smaller detectors instead of big detector and there are reasons for this. Firstly, smaller detector has better resolution. Secondly, the interactions are reduced in smaller detector, which provide a chance to use stronger source. The third reason is that we use four smaller detectors instead of one. As we can see in the above results, if we use only one smaller detector, the MDL won't improve so much.

For the comparison of the cloverleaf system with the modified standard system, if we fix the detector source distance to 16mm, and change the source detector distance from 30mm to 25mm, 22mm and 20mm, the MDL would decrease as distance decreased (table 2-10, table 2-12). This is because there's a collimator around the source. The radius of the source is 1.5mm, while the inner radius of the collimator is 1.5mm, the outer radius of the collimator is 5.0mm and the length of the collimator is 3mm. When the source detector distance is bigger, the emitting range to the phantom would be larger and there would be more Compton scattering background from the phantom, which leads to a higher MDL. This effect is more evident for the old phantom in leg phantom since the leg phantom is much bigger than a bare phantom. That's why the change of the ratio for the old phantom in leg phantom measurement is bigger than that for the bare phantom measurement.

By using modified standard system we compared the cloverleaf system and the conventional system at the same geometries. We got a conclusion that the MDL would be

most improved at the geometry (DS=20mm, SS=4mm), where the ratio of the MDL is about 0.409 for the bare phantom and 0.423 for the old phantom in leg phantom. By comparing the modified standard system with standard system, we got a geometrical improvement factor which listed in table 2-17 and table 2-18. In the tables, we can see the biggest geometrical improvement occurred at geometry (20,4). The values are 0.821 for bare phantom and 0.658 for the old phantom in leg phantom, which give rise to an overall improvement of 0.336 and 0.278 for the bare phantom and the old phantom in leg phantom. So, for the in vivo measurement which simulated by the old phantom in leg phantom, we can improve the MDL by a factor of 0.658 only by changing the geometry of the system without changing the source strength. If we use the cloverleaf system as well as a stronger source, the factor would be reduced to 0.278. The result of these two tables also tells us that the geometrical factor affects the in vivo measurement more than it affects the bare phantom measurement. This is because the in vivo measurement at a further distance gives rise to a bigger background count from Compton (relative to the signal count) scattering under the x-ray energy.

Table 2-13 and table 2-14 list the results of the MDL improvement of the cloverleaf system compared directly with the standard system. The lowest ratio of MDL is about 0.8 by using the current source, which means an improvement of 20% would occur at the geometry (DS=20mm, SS=4mm) even without using a stronger source. For a stronger source, the normalized results were list in table 2-14. This time, the lowest ratio occurs at geometry (DS=30mm, SS=14mm). This is because for closer DS and SS distance, we can't increase the source strength as much as we do for a further DS and SS distance due

to the count rate throughout limitation of the detector. As we can see in table 2-14, at the geometry (DS=30mm, SS=14mm), the cloverleaf system will get the same dead time as the standard system if we increase the source strength by about 5.00 times and the MDL ratio for these two system would be about 0.424. At the geometry (DS=20mm, SS=4mm), the cloverleaf system will get the same dead time as the standard system if we increase the source strength by about 3.30 times and the MDL ratio for these two system would be about 0.463. So, in order to get a better MDL in geometry (DS=30mm, SS=14mm), we need to increase the source strength by 5.05 times. But in geometry (DS=20mm, SS=4mm), we can only increase the source strength by 3.34 times to get a ratio of 0.46. So, there's a choice: either use a stronger source to get a better MDL in a further distance or use a weaker source to get a little worse MDL which is still much better than the MDL of the standard system in a closer distance.

For the measurement of old phantom in leg phantom, the changing trend is similar while the ratio is less than the results for the bare new phantom (table 2-15 and table 2-16). This means that when the scattering exists i.e. in the in vivo measurement, the MDL would be improved more than that for the in vitro measurement. In table 2-16, the MDL ratio is about 0.388 at geometry (DS=30mm, SS=14mm) if we increase the source strength by 3.490 times. The MDL ratio is about 0.415 at geometry (DS=20mm, SS=4mm) if we increase the source strength by about 2.515 times. So it is the same as for the new bare phantom – if we want to get a better MDL, we need a stronger source.

Table 2-19 to 2-22 show the MDL ratio of cloverleaf system and standard system with two methods for the Monte Carlo simulation and the measurement. The first method normalized the MDL of cloverleaf system by coherent rate of the standard system, which refers to a similar dead time for all the four geometries. At this condition, geometry (30,14) is the best of the four geometries. The second method has two steps: first normalized the MDL of cloverleaf system by coherent rate of the corresponding modified standard system, then compare the MDL of the modified standard system with the standard system. The overall ratio is the product of these two ratios. Since there's no normalization at the second step, the dead time for the four geometries may not be the same, which means we may overestimate the improvement by driving the system to a high dead time (for closer geometries such as (20,4)) in this method. But if the system permits, this result shows that we can improve the MDL by a factor of 0.658 only by changing the geometry without using a stronger source, which has been illustrated previously.

In fact, we can estimate the improvement only by a simple deduction. We know that

$$\text{MDL} \propto \frac{1}{\sqrt{\text{coherent count}}}$$

For the cloverleaf system, we have four detectors and four electronics, which means a four times coherent count compared to the conventional system (with only one detector) can be produced. So this can give rise to an MDL improvement by a factor of 0.5. Moreover, the smaller detector has a better resolution.

Since $\text{MDL} \propto \sqrt{\text{background}} \propto \sqrt{\text{resolution}}$ and the resolutions for the 8 mm radius detector and the 25 mm radius detector are 550 and 750 respectively. Combining these two factors, an improvement factor of $0.5 \times \sqrt{550} / \sqrt{750} = 0.428$ can be obtained, which

is quite similar to what we got from the simulations and measurements without considering the geometry factor.

According to Chettle D R et al.'s research in 1991, for in vivo tibia measurements, the typical precision (one standard deviation) is around 5 micrograms lead/(g bone mineral), which gives rise to a MDL of around 10 micrograms lead/(g bone mineral). In a research by Hoppin J A et al. in 1997, 168 teenagers' tibia were measured and the standard deviation is around 4.4 micro g lead/(g bone mineral), which gives rise to a MDL of around 8.8 micrograms lead/(g bone mineral). These measurements were done by the conventional system. If we use the cloverleaf system, the MDLs would be greatly improved.

The lead research members of Medical Physics group in McMaster University did a survey last summer (Aug., 2000) in Spokane, in which 73 persons were measured for both tibia and calcaneus. The measurements were done by the conventional system. The average MDLs (estimated by $2 \times \text{uncertainty}$) are 10.96 ± 5.98 micro g Pb/(g bone mineral) and 14.16 ± 3.96 micro g Pb/(g bone mineral) for the tibia measurement and calcaneus measurement respectively. If we use the cloverleaf system, the MDLs would be $0.278 \times (10.96 \pm 5.98) = (3.047 \pm 1.662)$ micro g Pb/g bone mineral and $0.278 \times (14.16 \pm 3.96) = (3.936 \pm 1.101)$ micro g Pb/(g bone mineral) for tibia and calcaneus respectively. It is a significant improvement.

3.1 Introduction

From the introduction of chapter 1, we know that the coherent scattering cross section depends upon incident energy E , angle of scatter θ and atomic number Z of the scattering element:

$$d\sigma = \frac{1}{2} r^2 (1 + \cos^2 \theta) |F(K)|^2 d\Omega \dots\dots\dots(3-1)$$

The atomic form factor $F(K)$ is a function of Z , E and θ . For the measurement of the lead in bone using ^{109}Cd , the energy of the coherent scattered photon is 88.035 keV and the K-edge energy of lead is 88.005. For the energy of interest, 88.035, and the mean scattering angle ($\sim 160^\circ$), the coherent scatter cross section varies approximately as Z^5 for $Z \leq 20$ (Chettle D R et al., 1991). As a result, approximately 99% of the coherent scatter signal in the lead XRF spectrum is due to the high Z bone mineral elements, as opposed to the low Z elements in the soft tissue surrounding the bone. We know that the lead K x-ray signals are the result of the interactions with photons which have an energy greater than the K-edge of lead which is 88.005keV. These photons consist of the photons emitted from the source and those undergo Compton scattering through less than 3.6° scattering angle. Since the fraction of the latter is negligibly small (Somervaille L J et al., 1985), we can consider that lead x-ray signals were totally created from the interaction of the lead with the uncollided γ -rays from ^{109}Cd source. So both of the coherent scatter signals and the lead K x-ray signals are due to the same ^{109}Cd source γ -rays. Therefore the ratio of the number of lead K x-ray signals over the number of the coherent signals can be

normalized to the ratio of lead concentration in bone mineral (micro g Pb/g bone mineral).

In principle, if we have a standard sample for which the composition is similar to the composition of bone and for which we know the concentration of the lead (micro g Pb/g bone mineral), we can obtain the concentration of a bone sample by measuring both of them. The way is to get the ratio

$$\left(\frac{KX - raySignal}{CoherentSignal} \right)_{sample} / \left(\frac{KX - raySignal}{CoherentSignal} \right)_{standard}$$

and then multiply the ratio by the lead concentration of the standard. But in practice, we use several phantoms as standards to get a more accurate calibration line. That is, we get the ratios of K x-ray signal/coherent signal for different lead concentrations and plot a calibration line of K x-ray signal/coherent signal versus lead concentrations (ppm). So for any sample, if we can get the K x-ray signal/coherent signal ratio, we can obtain the lead concentration from the line.

Usually we use plaster of Paris as the matrix material and add certain amounts of Pb to make the phantoms for different Pb concentrations. The composition of the plaster of Paris is usually $\text{CaSO}_4 \cdot 1/2\text{H}_2\text{O}$ and it is changed to $\text{CaSO}_4 \cdot 2\text{H}_2\text{O}$ during the creation of the phantom since we need to add some water into the material to make the concentration of the lead in the material be uniform. We have two sets of phantoms in our Laboratory now and we call them old phantoms and new phantoms according to the date of their creation. We found that the calibration lines of the K_β peaks for these two sets of phantoms were not the same. Since the calibration line is very important for the

determination of the lead concentration, it's necessary to find the reason for the different calibration lines. Since the old phantoms have been used as standards for several years and always give rise to good results, there must be some problem with the new phantoms. Also in this work, we want to find out how the resolution affects the K_{β} x-ray peaks by changing the resolution of the system.

3.2 spectrum fitting

Mqerfa is a program used to analyse the XRF spectrum and to calculate the lead concentration in bone. As I mentioned above, the principle for lead concentration calculation is to find the relationship between the ratio of the K x-ray signals to the coherent signals and the concentration of the lead by unit of micro g Pb/g bone mineral. So it's essential for us to get accurate K x-ray signals and coherent signals for the phantoms and the samples. The lead K x-rays have five different energies and we call them $K_{\alpha s}$ and $K_{\beta s}$. Since there are some other interactions that produce photons whose energy are similar to the energy of $K_{\alpha s}$, $K_{\beta s}$ and coherent scattered photons, the peaks of K_{α} x-rays, K_{β} x-rays and coherent photons are not pure peaks for the corresponding energies. Hence we can't get the K x-ray signal counts and coherent signal counts directly from the spectrum. So an important procedure in the Mqerfa program is fitting the spectrum to get more accurate K x-ray signal and coherent signal counts. There are alpha-fitting, beta-fitting and coherent fitting routines for different peaks.

3.2.1 Coherent fitting

If we have a monoenergetic peak located at channel A with amplitude B, then the distribution of this peak would be:

$$f(x) = B \times e^{-\left(\frac{x-A}{\sqrt{2}\sigma}\right)^2} \dots\dots\dots(3-2)$$

where σ is the standard deviation and x is the channel number.

The energy of the coherent peak is 88.035. The fit is conducted over an energy interval of approximately 86.5 keV to 89.5 keV. There are several sources that can contribute to this energy region which include:

- a. The contribution of Lead $K_{\beta 2}'$ and $K_{\beta 2}''$ x-rays.

The energy of $K_{\beta 2}'$ x-ray is 87.367keV and the energy of $K_{\beta 2}''$ is 87.233keV.

Their distributions can be expressed by normal distribution.

- b. The contribution of the background.

The background is exponentially distributed, so it can be expressed as an exponential function.

- c. The contribution of O K edge (~87.504keV), Ca L edge (~87.65keV), C K edge (~87.752keV) and P/S L edge (~87.9keV and ~87.8keV). Where the edge, in each case, is the upper energy limit of the Doppler broadened distribution of Compton scattering from the electron shell.

- d. Because of incomplete charge collection, there is a step in the coherent peak and $K_{\beta 2}$ peak, which can be expressed by a complementary error function $\text{erfc}(x)$ derived from error function $\text{erf}(x)$, where x is the Gaussian parameter $(x - \mu) / \sqrt{2}\sigma$. The different identities in c above are closely similar in energy and

are also similar in energy to both the $K_{\beta 2}$ x-rays and the coherent peak. In practice they are accounted for by a step which is larger than would it be for an isolated peak.

So the coherent peak can be expressed the following function with some variables which

$$f(x) = A(2) \times \left(\exp\left(-\left(\frac{x - A(1)}{A(3)}\right)^2\right) + A(7) \times \operatorname{erfc}\left(\frac{x - A(1)}{A(3)}\right) \right) + A(4) \times \left(\exp\left(-\left(\frac{x - (A(1) - 668 / G)}{A(3)}\right)^2\right) + A(7) \times \operatorname{erfc}\left(\frac{x - (A(1) - 668 / G)}{A(3)}\right) \right) + 0.509 \times \left(\exp\left(-\left(\frac{x - (A(1) - 802 / G)}{A(3)}\right)^2\right) + A(7) \times \operatorname{erfc}\left(\frac{x - (A(1) - 802 / G)}{A(3)}\right) \right) + A(5) \times \exp(A(6)x) \dots \dots \dots (3 - 3)$$

are going to be fitted in the program.

where

A(1) is the position of coherent;

A(2) is the amplitude of coherent;

A(3) is the width of coherent which can be estimated by $\sqrt{2}\sigma$ which equals to $\sqrt{2}FWHM / 2.355$;

A(4) is the amplitude of $K_{\beta 2}'$;

A(5) is the amplitude of exponential background;

A(6) is the exponent coefficient of exponential background;

A(7) is the step height (expressed as a fraction of peak height).

Here, the positions of $K_{\beta 2}'$ and $K_{\beta 2}''$ are fixed with respect to the coherent position A(1) by $A(1) - 668 / G$ and $A(1) - 802 / G$ where G is the gain in units of eV/channel, which can be obtained from the spectrum energy calibration line (gain is the slope of the energy calibration line). 668 is the energy difference between coherent peak and $K_{\beta 2}'$ peak with a

unit of ev (88.035keV-87.367keV=668ev). G is the gain of the spectrum with a unit ev/channel. So 668/G is the number of channels between the coherent peak and $K_{\beta 2}'$ peak. 802ev is the energy difference between the coherent peak and $K_{\beta 2}''$ peak while 802/G is the number of channels between the coherent peak and $K_{\beta 2}''$ peak.

Least squares fit to an arbitrary function

Now that we know the function of the coherent peak, the next step is how to fit the measurement spectrum with this function. The most frequently used method is the least squares fitting method. Philip R. Bevington described the least squares fit method in detail in the book “Data Reduction and Error Analysis for the Physical Sciences”.

Assume we have a function $y(x)$ with parameters $A(j)$ as the function for the coherent peak described above.

$$\begin{aligned}
 y(x) = & \\
 & A(2) \times \left(\exp\left(-\left(\frac{x - A(1)}{A(3)}\right)^2\right) + A(7) \times \operatorname{erfc}\left(\frac{x - A(1)}{A(3)}\right) \right) + \\
 & A(4) \times \left(\exp\left(-\left(\frac{x - (A(1) - 668 / G)}{A(3)}\right)^2\right) + A(7) \times \operatorname{erfc}\left(\frac{x - (A(1) - 668 / G)}{A(3)}\right) \right) + \\
 & 0.509 \times \left(\exp\left(-\left(\frac{x - (A(1) - 802 / G)}{A(3)}\right)^2\right) + A(7) \times \operatorname{erfc}\left(\frac{x - (A(1) - 802 / G)}{A(3)}\right) \right) + \\
 & A(5) \times \exp(A(6)x) \dots \dots \dots (3-4)
 \end{aligned}$$

We can define a measure of goodness of fit X^2

$$X^2 \equiv \sum \left\{ \frac{1}{\sigma_i^2} [y_i - y(x_i)]^2 \right\} \dots \dots \dots (3-5)$$

where the σ_i are the uncertainties in the data points y_i . According to the method of least squares, the optimum values of the parameters $A(j)$ are obtained by minimizing X^2 with respect to each of the parameters simultaneously.

$$\frac{\partial}{\partial A(j)} X^2 = \frac{\partial}{\partial A(j)} \sum \left\{ \frac{1}{\sigma_i^2} [y_i - y(x_i)]^2 \right\} = 0 \dots\dots\dots (3-6)$$

The method of least squares consists of determining the values of the parameters $A(j)$ of the function $y(x)$ which yield a minimum for the function X^2 given above. There are a number of ways of finding this minimum value. If the variation of X^2 with each parameter $A(j)$ is fairly independent of how well optimized the other parameters are, then the optimum values can be determined most simply by minimizing X^2 with respect to each parameter separately. This is the method of the grid search.

The grid search is the most basic method for least-square fitting. But in practice, all the parameters $A(j)$ are incremented simultaneously, with the relative magnitudes adjusted so that the resultant direction of travel in parameter space is along the gradient (i.e. the direction of maximum variation) of X^2 . This method is called the gradient-search method. In this program, we make a least-squares fit to a function using the algorithm of Marquardt which combines a gradient search with an analytical solution developed from linearizing the fitting function.

The optimum values of the parameters $A(j)$ are obtained by minimizing X^2 with respect to each of the parameters simultaneously, which can be expressed as equation(3-6). In

order to solve the equation $\frac{\partial}{\partial A(j)} X^2$, two matrices alpha and beta matrices, are to be evaluated. The alpha matrix is a symmetrical curvature matrix, which measures the curvature of the X^2 hypersurface and the beta matrix is a row matrix. They can be derived from the first-order expansion of X^2 and can be expressed as following:

$$\alpha_{j,k} = \sum \frac{1}{\sigma_i^2} \frac{\partial y(x_i)}{\partial A(j)} \frac{\partial y(x_i)}{\partial A(k)} \dots\dots\dots (3-7)$$

$$\beta_k \equiv \sum \left\{ \frac{1}{\sigma_i^2} [y_i - y_0(x_i)] \frac{\partial y_0(x_i)}{\partial A(k)} \right\} \dots\dots\dots (3-8)$$

The Marquardt algorithm can be obtained by increasing the diagonal terms of the curvature matrix alpha by a factor λ which controls the interpolation of the algorithm between the two extremes. So the two matrices become

$$\beta = \delta A \alpha'$$

$$\alpha'_{jk} = \begin{cases} \alpha_{jk}(1 + \lambda) & \text{for } j = k \dots\dots\dots (3-9) \\ \alpha_{jk} & \text{for } j \neq k \end{cases}$$

The solution for the parameter increments $\delta A(j)$ from the above equations would be

$$\delta A(j) = \sum_{k=1}^n (\beta_k \epsilon'_{jk}) \dots\dots\dots (3-10)$$

where the matrix ϵ' is the inverse of the matrix α' .

The procedure to solve A is:

1. Compute $X^2(A)$.
2. Start initially with $\lambda = 0.001$.
3. Compute δA and $X^2(A + \delta A)$ with this choice of λ .
4. If $X^2(A + \delta A) > X^2(A)$, increase λ by a factor of 10 and repeat step (3).

5. If $X^2(A+\delta A) < X^2(A)$, decrease λ by a factor of 10, consider $A'=A+\delta A$ to be the new starting point, and return to step (3) substituting A' for A .
6. If the X^2 increases and ΔX^2 is less than or equal to a limit (such as 1×10^{-3}), then the difference is insignificant and we use this X^2 as the final X^2 and the parameters for this X^2 are the final parameters.

That's the whole procedure of fitting and it also fits for alpha and beta fittings which would be described in the following sections. For detail explanation, please refer to the book "Data reduction and error analysis for the physical sciences".

3.2.2 Alpha fitting

The energies of $K_{\alpha 1}$ and $K_{\alpha 2}$ are 74.969keV and 72.804keV respectively. Since the energies are very close, we fit them with $K_{\alpha 1}$, and add the contribution of $K_{\alpha 2}$ by multiplying by a fixed factor. Since the background beneath $K_{\alpha 1}$ and $K_{\alpha 2}$ x-ray peaks has a Compton component which decreases rapidly with increasing energy, the background is expressed by two exponential functions. So four other parameters are needed to include the background contributions.

The function of the $K_{\alpha 1}$ peak would be like this:

$$f(x) = A(2) \times \left(\exp\left(-\left(\frac{x - A(1)}{W}\right)^2\right) + H \times \operatorname{erfc}\left(\frac{x - A(1)}{W}\right) \right) + (0.593 \times A(2)) \times \left(\exp\left(-\left(\frac{x - (A(1) - 2165/G)}{W}\right)^2\right) + H \times \operatorname{erfc}\left(\frac{x - (A(1) - 2165/G)}{W}\right) \right) + A(3) \times \exp(A(4) \times x) + A(5) \times \exp(A(6) \times x) \dots \dots \dots (3-11)$$

where

$A(1)$ is the position of lead $K_{\alpha 1}$;

A(2) is the amplitude of lead $K_{\alpha 1}$;

A(3) is the amplitude of exponential background1;

A(4) is the exponent coefficient of exponential background1;

A(5) is the amplitude of exponential background2;

A(6) is the exponent coefficient of exponential background2.

W and H are width and step height, which can be fixed by the best fit parameters A(3) and A(7) got from coherent fitting.

2165ev is the energy difference between $K_{\alpha 1}$ peak and $K_{\alpha 2}$ peak and 2165/G is the number of channels between the $K_{\alpha 1}$ peak and $K_{\alpha 2}$ peak.

The fitting procedure is the same as the coherent fitting.

3.2.3 Beta fitting

The energies of $K_{\beta 1}$, $K_{\beta 2}$ and $K_{\beta 3}$ are 84.936keV, 87.300keV and 84.450keV. The $K_{\beta 2}'$ and $K_{\beta 2}''$ are fitted by the algorithm that models the coherent peak, but proximity to K edges from O and C and L edges from Ca and P (or S), which are not explicitly modeled, makes estimates of $K_{\beta 2}$ amplitudes unreliable. Moreover, the yield of this x-ray is small. So no attempt is made to use this information in estimating lead concentration. The energies of $K_{\beta 1}$ and $K_{\beta 3}$ are very close, so we fit them with $K_{\beta 1}$, and add the contribution of $K_{\beta 3}$ just as we do in alpha fitting. There are some other sources can contribute to the $K_{\beta 1}$ peak which include:

- a. The contribution of the background;
- b. The contribution of the Ca K edge ($\sim 83.997\text{keV}$);

- c. The contribution of the P K edge (~85.889keV) (only for in vivo, not for phantoms);
- d. The contribution of the S K edge (~85.288keV) (only for the phantoms);
- e. For each peak, there is a step due to incomplete charge collection.

So the counts for every channel among the peak area would be:

The contribution of $K_{\beta 1}$ + the contribution of $K_{\beta 3}$ + the contribution of the background + the contribution of Ca edge + the Contribution of S edge or the Contribution of P edge

Therefore the function of $K_{\beta 1}$ peak for phantoms can be expressed as following:

$$\begin{aligned}
 f(x) = & A(1) \times \left(\exp\left(-\left(\frac{x - (CPOS - 3099/G)}{W}\right)^2\right) + H \times \operatorname{erfc}\left(\frac{x - (CPOS - 3099/G)}{W}\right) \right) + \\
 & (0.523 \times A(1)) \times \left(\exp\left(-\left(\frac{x - (CPOS - 3585/G)}{W}\right)^2\right) + H \times \operatorname{erfc}\left(\frac{x - (CPOS - 3585/G)}{W}\right) \right) + \\
 & A(2) \times \exp(A(3) \times x) + 0.030 \times CO1 \times \exp(A(4) \times POSCA) \times \operatorname{erfc}\left(\frac{POSCA}{W}\right) + \\
 & 0.44 \times \exp(A(4) \times POSS) \times \operatorname{erfc}\left(\frac{POSS}{W}\right) \dots \dots \dots (3-12)
 \end{aligned}$$

where

A(1) is the amplitude of $K_{\beta 1}$;

A(2) is the amplitude of exponential background;

A(3) is the exponent coefficient of exponential background;

A(4) is the exponential on calcium and phosphorus edges;

CPOS, H, W and CO1 are coherent position, step height, width and coherent peak amplitude, which can be fixed by the best fit parameters A(1), A(7), A(3) and A(2) got from the coherent fitting;

POSCA is the position of Ca edge, which equals to $(x - (CPOS - 4038/G))$;

POSS is the position of S edge, which equals to $(x - (CPOS - 2747/G))$;

4038ev is the energy difference between the coherent peak and Ca edge, so 4038/G is the number of channels between the coherent peak and Ca edge;

2747ev is the energy difference between the coherent peak and S edge, so 2747/G is the number of channels between the coherent peak and S edge.

The above function is the function of $K_{\beta 1}$ peak for phantoms and the function of $K_{\beta 1}$ peak for people can be expressed as following (the difference is that there's a P edge in the beta peak for people instead of the S edge for that of the phantoms):

$$\begin{aligned}
 f(x) = & A(1) \times \left(\exp\left(-\left(\frac{x - (CPOS - 3099/G)}{W}\right)^2\right) + H \times \operatorname{erfc}\left(\frac{x - (CPOS - 3099/G)}{W}\right) \right) + \\
 & (0.523 \times A(1)) \times \left(\exp\left(-\left(\frac{x - (CPOS - 3585/G)}{W}\right)^2\right) + H \times \operatorname{erfc}\left(\frac{x - (CPOS - 3585/G)}{W}\right) \right) + \\
 & A(2) \times \exp(A(3) \times x) + 0.040 \times CO1 \times \exp(A(4) \times POSCA) \times \operatorname{erfc}\left(\frac{POSCA}{W}\right) + \\
 & 0.21 \times \exp(A(4) \times POSP) \times \operatorname{erfc}\left(\frac{POSP}{W}\right) \dots \dots \dots (3-13)
 \end{aligned}$$

where all the parameters are the same as the function for phantoms. Here POSP refers to the position of P edge and it equals to $(x - (CPOS - 2146/G))$. 2146ev is the energy difference between the coherent peak and P edge, so 2146/G is the number of channels between the coherent peak and P edge.

In the function, we tied the amplitude of the Ca, S and P edge to the amplitude of the coherent. From the previous description about the normalization of the lead by the coherent peak, we can learn that the amplitude of the Ca, S and P edge change proportionally to the amplitude of the coherent amplitude. Since the Ca, S and P concentrations are the same for the same set of phantoms as well as for the human bones, the ratios of the three edges to the coherent amplitude can be determined by measurement or by calculation using the published parameters. The ratios of Ca edge/Coh amplitude

and S edge/Ca edge are set to be 0.03 and 0.44 in the original program for phantoms. The ratios of Ca edge/Coh amplitude and P edge/Ca edge are set to be 0.04 and 0.21 for people. As mentioned above, there's some problem with the calibration line of the beta fitting. Since the quality of beta fitting is decided by these parameters, there may be some problem with these parameters. We'll illustrate this in detail at the following sections.

3.3 The calibration line for old and new phantoms

The system used in this work is similar to the standard system used in the previous work except that some of the parameters were modified in this work.

The set up of the parameters is listed in table 3-1.

Amplifier		Shaping time (μ s)	ADC (channel)
Fine gain 0.634	Coarse gain 100	4, 2, 1, 0.5	2048

Table 3-1 system setup parameters

The resolution of this system is about 570ev, 620ev, 730ev and 870ev corresponding to the shaping time 4, 2, 1, and 0.5 μ s.

As mentioned above, the purpose of this work is to find the problem with the beta calibration line and to find how resolution affects the ratio of those edges to the coherent edge. So we need to do some little modifications for the beta-fitting program.

First, let's have a look at the beta-fitting calibration lines for the old and new phantoms. Figure 3-1 shows the beta-fitting calibration lines obtained by using old phantoms and new phantoms respectively.

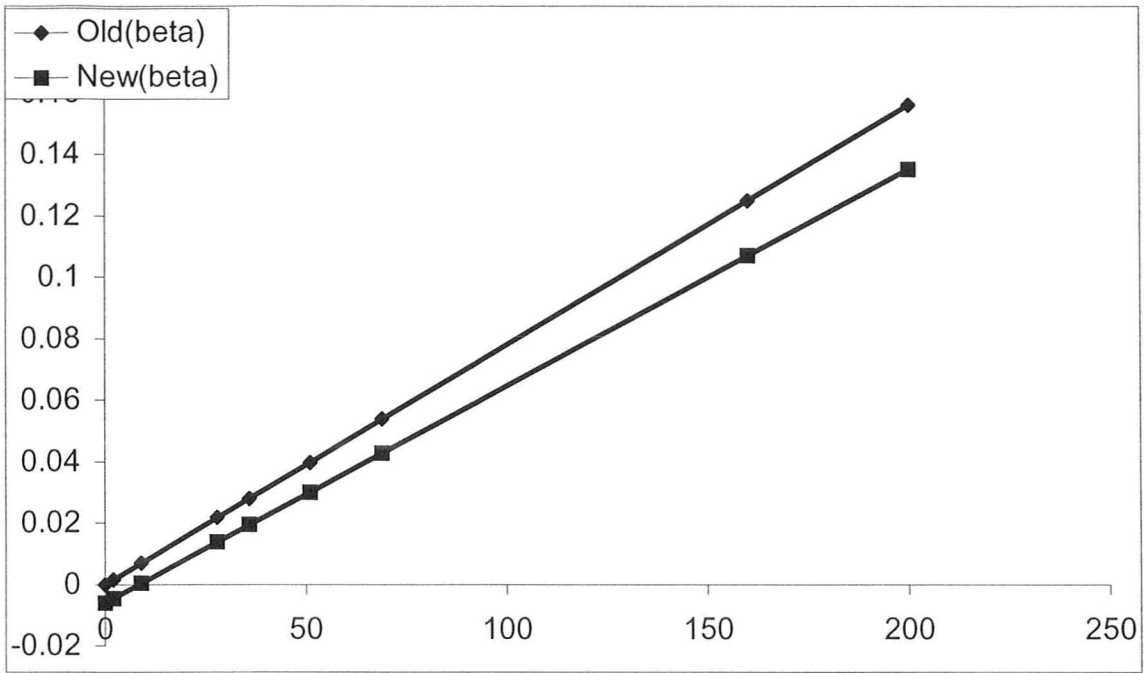


Figure 3-1 The beta calibration lines for old and new phantoms

The functions of these two lines are

$$\left(\frac{Beta}{Coh}\right)_{Old} = (0.00078096 \pm 0.00001297) \times x(ppm) - (0.00006135 \pm 0.0011587) \quad (t < 0.0001)$$

$$\left(\frac{Beta}{Coh}\right)_{New} = (0.00070584 \pm 0.00000827) \times x(ppm) - (0.00590493 \pm 0.00068417) \quad (t < 0.0001)$$

.....(3-14)

In the above equations, beta/coh is the ratio of the counts of the beta peak and the counts of the coherent peak.

There is an abnormal negative interception for new calibration line and also the slope of the new calibration line is about 10% lower than that of the old calibration line.

We also observed that the slope of the alpha calibration line for the new phantoms is about 10% lower than that of the old phantoms however there was not a similar discrepancy in the intercept. So for the same ppm, the ratio beta/coh for old phantoms is bigger than that of the new phantoms. Since the cross-section for the K_{β} x-ray of lead is always the same, the cross-section of the coherent scattering must have changed. For the same concentration, the coherent peak for old phantoms is smaller than that of the new phantoms, so the cross-section of the coherent scattering for the new phantoms is bigger than that of the old phantoms. The cross-section of the coherent scattering depends on the concentration of the high Z elements of the phantoms, so the concentration of the high Z elements in these two sets of phantoms must be different.

For the abnormal negative interception, we can explain it this way. Remember when we do the beta fitting, the total count at the energy of beta peak is equals to the addition of the count of K_{β} x-rays, Ca edge, S edge and background. The negative interception means we underestimate the count of K_{β} x-rays, that is, we overestimate the count of the Ca edge and S edge. Since we fixed the count of Ca edge and S edge to coherent counts, the fixed parameters for these edges must be different for these two sets of phantoms. We'll analyze this by detail in the following sections.

3.4 The composition of the new phantom

3.4.1 The results from the fitting program

Three old phantoms, three new phantoms and a bare bone (with three detection positions) were measured for different resolutions. Each of them measured for about 10 hrs and the results were analyzed.

In original program we have 4 parameters for beta fitting: The amplitude of beta1, the amplitude of exponential background, the exponent coefficient of the background and the exponential on Ca, P and S edges. For the investigation of the phantoms, we don't need to worry about P edge which only appears in in vivo measurements. The ratios of Ca edge to coherent amplitude and the S edge amplitude to Ca edge amplitude are fixed in the original program. In order to investigate the character of the new phantoms, we floated these two ratios, i.e. added two parameters in the fitting program to let the program determine the value of these two ratios. Table 3-2 lists the Ca/Coh and S/Ca ratios for the fitting of the spectra of 0ppm new phantom and old phantom.

New phantoms				Old phantoms			
filename	resolution	Ca/Coh	S/Ca	filename	resolution	Ca/Coh	S/Ca
new000a	577	0.0368	0.227	old000a	564	0.0258	0.527
new000b	624	0.0412	0.218	old000b	620	0.0331	0.509
new000c	703	0.0446	0.248	old000c	630	0.0356	0.386
				old000d	735	0.0396	0.453
	average	0.0409	0.231		average	0.0335	0.469
	stdev	0.0039	0.016		stdev	0.0058	0.064

Table 3-2 Ca/Coh and S/Ca ratios for the new phantoms and old phantoms

Note: the unit for the resolution is eV.

So the measured ratios for Ca/Coh and S/Ca are 0.0409 ± 0.0039 and 0.2310 ± 0.0158 for the new phantoms. The measured ratios for Ca/Coh and S/Ca are 0.0335 ± 0.0058 and 0.4687 ± 0.06361 for the old phantoms. In the original program, the ratios of Ca/Coh and S/Ca we used are 0.030 and 0.44. So the ratios for the old phantom are the same as that we used in the original program within the error, while the ratios for the new phantoms are quite different from that in the original program. As we can see from the table, the ratio of S/Ca for the new phantoms is about half of that for the old phantoms, which means the ratio of the concentration of S and Ca in new phantoms is about half of that in old phantoms. It can also be seen from the table that the Ca/Coh ratio is about 20% bigger for the new phantoms than that for the old phantoms. So we can conclude that the concentration of Ca in new phantoms is bigger than that in the old phantoms. The main composition of old phantoms is $\text{CaSO}_4 \cdot 2\text{H}_2\text{O}$. The composition of the new phantoms needs to be confirmed.

3.4.2 The results of neutron activation analysis (NAA)

To confirm the concentration ratio of S/Ca for the old phantoms and new phantoms, we analyzed the materials used to make these two sets of phantoms by NAA. We weighed two new phantom samples ($\text{CaSO}_4 \cdot 1/2\text{H}_2\text{O}$) and two old phantom samples ($\text{CaSO}_4 \cdot 2\text{H}_2\text{O}$) and irradiated them for 300 seconds. Then measured them for 600 seconds after 180 seconds' cooling. Table 3-3 lists the sample information and measurement result.

Sample ID	mass(mg)	Irr time(s)	Cool time(s)	Mea time(s)	S net count	Ca net count
New1	96.8	300	180	600	1131 ± 55	193967 ± 912
New2	95.9	300	180	600	1053 ± 54	190998 ± 898
Old1	104.8	300	180	600	2266 ± 67	145823 ± 787
Old2	106.6	300	180	600	2310 ± 69	154501 ± 803

Table 3-3 Sample information and measurement result for NAA

The concentration calculation formula for NAA is as following:

$$W = \frac{MA}{6.02 \times 10^{23} \theta \phi \sigma \gamma \epsilon S D C} \dots\dots\dots (3-15)$$

where

W is the concentration with unit mg;

M is the atom mass for the element with unit mg/mol;

A is the activity of the element after irradiation;

θ is the abundance of the isotope of the element before irradiation;

ϕ is the neutron flux;

σ is the cross-section of the reaction;

γ is the branch ratio of the reaction;

ϵ is the detector efficiency;

S is the saturation factor;

D is the decay factor;

C is the counting factor;

And

$$\begin{aligned} S &= 1 - \exp(-0.693t_1 / t) \\ D &= \exp(-0.693t_2 / t) \dots\dots\dots (3-16) \\ C &= (1 - \exp(-0.693t_3 / t)) / (0.693t_3 / t) \end{aligned}$$

where t_1 , t_2 and t_3 are irradiation time, cooling time and counting time respectively.

The factors needed for the calculation are listed in table 3-4.

reaction	atomic mass	cross-section	half-life	energy	abundance
48Ca(n, γ)49Ca	40.08	1.1b	8.72min	3084.4	0.19%
36S(n, γ)37S	32.06	0.16b	5.05min	3103.8	0.02%

Table 3-4 nuclear factors for the NAA of S and Ca element

So, for the new phantoms, the atoms of S / the atoms of Ca can be expressed as:

$$\begin{aligned} \left(\frac{S_{atom}}{Ca_{atom}}\right)_{new1} &= \frac{\frac{W_s}{M_s} \times 6.02 \times 10^{23}}{\frac{W_{Ca}}{S_{Ca}} \times 6.02 \times 10^{23}} = \frac{A_s}{A_{Ca}} \times \frac{\theta_{Ca}}{\theta_s} \times \frac{\sigma_{Ca}}{\sigma_s} \times \frac{S_{Ca} \times D_{Ca} \times C_{Ca}}{S_s \times D_s \times C_s} \\ &= \left(\frac{1131 \pm 55}{193967 \pm 912}\right) * \frac{0.19}{0.02} * \frac{1.1}{0.16} * \frac{0.17824}{0.17848} \\ &= 0.379 \pm 0.019 \end{aligned}$$

$$\left(\frac{S_{atom}}{Ca_{atom}}\right)_{new2} = 0.359 \pm 0.019$$

$$\text{So } \left(\frac{S_{atom}}{Ca_{atom}}\right)_{newaverage} = 0.369 \pm 0.015$$

$$\text{According to the same formula, } \left(\frac{S_{atom}}{Ca_{atom}}\right)_{oldaverage} = 0.992 \pm 0.027$$

So the ratio of $(S/Ca)_{old}/(S/Ca)_{new}$ can be expressed as:

$$\frac{0.992 \pm 0.027}{0.369 \pm 0.015} = 2.69 \pm 0.13$$

The ratios of Sedge/Caedge for old phantoms and new phantoms obtained from the fitting program are 0.4687 ± 0.06361 and 0.2310 ± 0.0158 , so the ratio of $(S/Ca)_{old}/(S/Ca)_{new}$ from these two ratios is 2.03 ± 0.31 . The average value is 2.36 ± 0.47 .

In this experiment, some Sulfur standard also has been irradiated and analyzed. From the results, the composition of Sulfur is around 9% (0.090 ± 0.004).

3.4.3 The results of Guelph chemical laboratories LTD.

To confirm the composition of the other elements in new phantoms, we sent some samples to the Guelph chemical laboratories LTD. Table 3-5 lists the analysis result.

ELEMENT	CONCENTRATION (PPM)
Aluminum	55.0; 58.1
Barium	15.6; 15.6
Boron	20.2; 17.9
Calcium	32.6%; 32.2%
Iron	601; 550
Magnesium	2572; 2198
Manganese	72.1; 66.2
Phosphorus	7.0; 8.2
Sodium	278; 224
Strontium	719; 693
Carbon	5.14%; 5.25%
Sulfur	8.24%; 8.04%

Table 3-5 element concentrations of new phantoms obtained from chemical analysis

Assuming the main components of the new phantoms are CaCO_3 and $\text{CaSO}_4 \cdot 1/2\text{H}_2\text{O}$, which are the main components of the plaster of Paris used to make the new phantoms. Then the proportion of $\text{CaSO}_4 \cdot 1/2\text{H}_2\text{O}$ can be calculated from the concentration of Carbon (about 5.2%), Calcium (32.4%) and Sulfur (8.14%), which is around 56.55%, 58.34% and 36.9% respectively. The average value is 0.506 ± 0.119 .

Summarizing the results got from fitting, NAA and Chemical analysis, the ratios for $(S_{\text{atom}}/Ca_{\text{atom}})_{\text{new}}$ are 0.493 ± 0.101 , 0.369 ± 0.015 and 0.419 ± 0.139 respectively. The average value is 0.427 ± 0.062 .

Assuming the weight proportions of $\text{CaSO}_4 \cdot 1/2\text{H}_2\text{O}$ and CaCO_3 in the plaster of Paris powder (which was used to make new phantoms) are 50.6% and 49.4% respectively, then the weight proportions of $\text{CaSO}_4 \cdot 2\text{H}_2\text{O}$ and CaCO_3 in the new phantoms would be

54.85% and 45.15%. Also assuming only $\text{CaSO}_4 \cdot 2\text{H}_2\text{O}$ exists in the old phantoms. By calculating the coherent cross section for both new phantoms and old phantoms and comparing them, we found the coherent cross section of the new phantom is around 11.83% bigger than that of the old phantom. This is the reason why the slopes of the alpha calibration line and beta calibration line for the new phantom is about 10% lower than those of the old phantoms.

3.5 How resolution affects the Ca (S) edge

3.5.1 relationship between resolution and Ca edge/coh peak

We can see from the results that the Ca/Coh ratio change with the change of resolution.

Table 3-6 lists the resolutions and the Ca/Coh ratios.

Resolution	Ca/Coh
564	0.0278
568	0.0305
578	0.0322
577	0.0292
568	0.0284
620	0.0353
630	0.0338
630	0.0336
619	0.0303
624	0.0329
626	0.0325
622	0.0279
735	0.0397
740	0.0434
706	0.0352
703	0.0411
742	0.0384
738	0.0393
866	0.0474
868	0.0494
870	0.0483
869	0.0488
872	0.0435
875	0.0408

Table 3-6 the resolutions and their corresponding Ca edge/Coh peak ratio

The Ca/Coh versus resolution curve can be illustrated as figure 3-2:

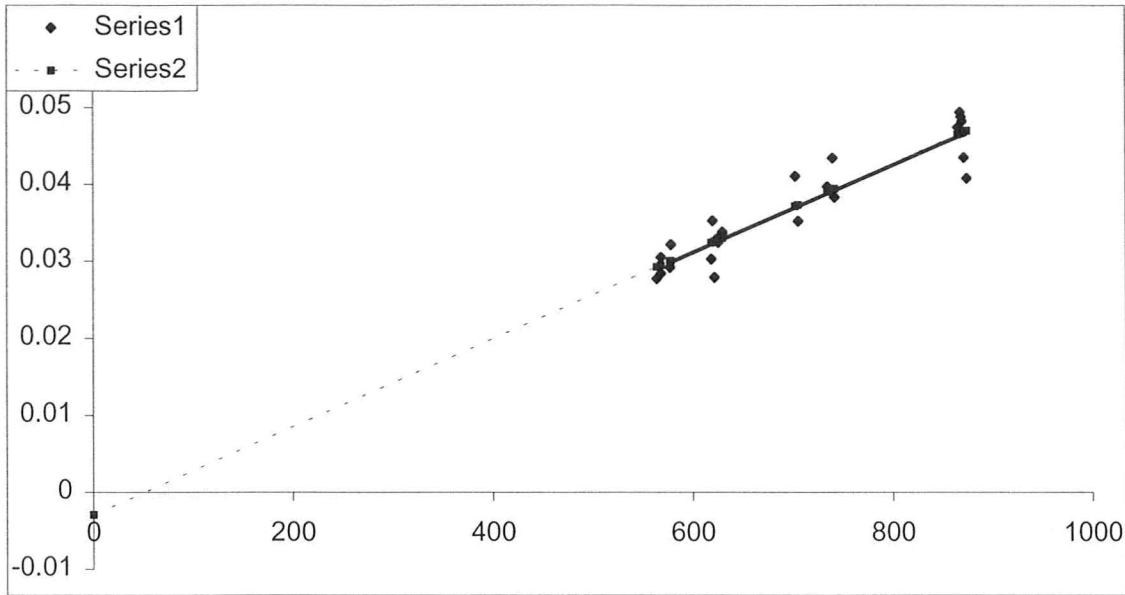


Figure 3-2 Ca edge/Coh peak versus resolution

The function of this curve is:

$$\frac{Ca}{Coh} = (5.7075 \times 10^{-5}) \times resolution - 0.0029 (t < 0.0001) \dots\dots\dots (3-17)$$

So Ca/Coh has a linear relationship with the resolution, hence the resolution would affect the result of analysis. When we expand the line to the point when the resolution is zero, the ratio Ca/Coh is close to zero, which makes sense – as the resolution goes to zero, the coherent peak goes to infinity, so the Ca/Coh peak tends to zero.

3.5.2 relationship between resolution and Ca edge/(coh peak*FWHM)

In the above section, the Coh in Ca/Coh means the coherent peak. The effect of increasing resolution is to broaden the peak, which directly relates to the FWHM of the peak. If we use Ca/(Coh*FWHM), this effect could be eliminated.

Table 3-7 lists the resolution and Ca/(Coh*FWHM) ratios. FWHM equals resolution. But for the convenience of calculation, we use FWHM'=FWHM/1000, i.e. use keV as unit instead of eV.

resolution	ca/(coh*FWHM)	Z
564	0.0492	-1.0016
568	0.0537	0.2547
578	0.0557	0.8107
577	0.0507	-0.6076
568	0.0500	-0.7848
620	0.0569	1.1404
630	0.0537	0.2438
630	0.0534	0.1616
619	0.0489	-1.0858
624	0.0527	-0.0328
626	0.0519	-0.2588
622	0.0449	-2.2182
735	0.0540	0.3347
740	0.0587	1.6426
706	0.0499	-0.8111
703	0.0584	1.5729
742	0.0517	-0.3160
738	0.0533	0.1292
866	0.0548	0.5455
868	0.0569	1.1437
870	0.0555	0.7390
869	0.0562	0.9371
872	0.0499	-0.8095
875	0.0466	-1.7298

Table 3-7 the resolutions and their corresponding Ca edge/Coh*FWHM ratios

Note: Column Z refers to the z-value which obtained from $(x-\mu)/\sigma$, where x are the values of ca/(coh*FWHM), μ is the average of these values and σ is the standard error of these values.

The Ca/(Coh*FWHM) versus resolution curve can be illustrated as figure 3-3:

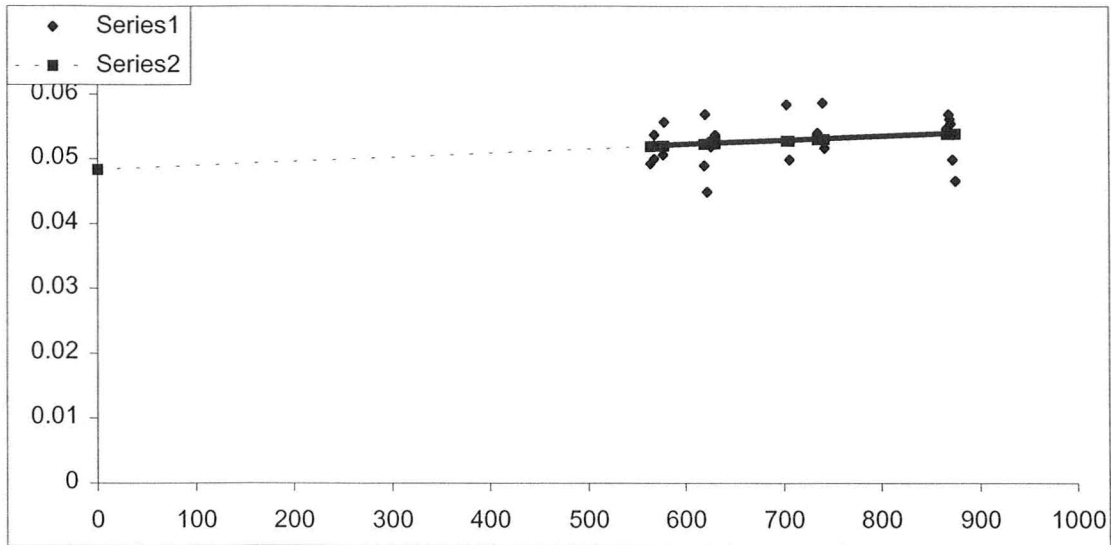


Figure 3-3 Ca edge/(Coh*FWHM) versus resolution

The t-test value for this curve is 0.9777 which means that the probability for the slope equals zero is greater than 60%. So we can say the ratio Ca/(Coh*FWHM) is independent of resolution. Moreover, from the table 3-7, the frequencies of z-values are distributed normally for all four sets of resolutions, which means the value of ca/(coh*FWHM) is not affected by the resolution. Therefore it's better to change the ratio Ca/Coh to Ca/(Coh*FWHM) in the program. It is the same with all the other ratios related with the Coherent amplitude.

3.6 results for bare bone

In this work, a bare tibia was measured in three positions and the positions were distributed as figure 3-4:

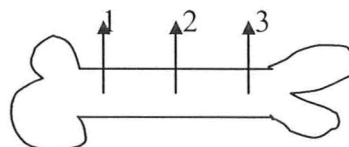


Figure 3-4 the positions of the bare tibia

Table 3-8 lists the ratios of beta/coh and beta/alpha for the three positions of the bare bone.

filename	beta/Coh	sigma	alpha/coh	sigma	bet/alph	sigma
bone1a	0.0110	0.0005	0.0535	0.0017	0.2050	0.0106
bone2a	0.0055	0.0005	0.0303	0.0018	0.1802	0.0193
bone3a	0.0130	0.0004	0.0632	0.0015	0.2061	0.0082
bone1b	0.0112	0.0004	0.0606	0.0014	0.1849	0.0076
bone2b	0.0062	0.0005	0.0427	0.0020	0.1446	0.0146
bone3b	0.0069	0.0004	0.0358	0.0014	0.1937	0.0128
bone1c	0.0073	0.0004	0.0518	0.0020	0.1412	0.0088
bone2c	0.0054	0.0007	0.0305	0.0032	0.1776	0.0287
bone3c	0.0053	0.0004	0.0334	0.0022	0.1594	0.0156

Table 3-8 ratios of beta/coh, alpha/coh, and beta/alpha for the three positions of the bare bone

Through calculation, we can get the average ratios of beta/coh, alpha/coh and beta/alpha for three positions and the values are listed in table 3-9.

parameter	position1	position2	position3
beta/coh	0.0098±0.0022	0.0057±0.0004	0.0084±0.0041
alpha/coh	0.0553±0.0047	0.0345±0.0071	0.0495±0.0150
beta/alpha	0.1770±0.0326	0.1675±0.0198	0.1864±0.0242

Table 3-9 average ratios of beta/coh, alpha/coh, and beta/alpha at three bone positions

We can see from the table that although the beta/coh and alpha/coh ratios are different in three positions, the ratio beta/alpha is the same for three positions within the error. This indicates that the concentration of the bone in different bone position is different, which means that the lead concentration in bone is not uniform and we should choose an optimal position for the measurement.

3.7 Discussion:

The calibration lines of the old phantoms and new phantoms were expressed by equation (3-14). The intercept of the old phantom is -0.00006135 , which gives rise to a lead concentration of about -0.08ppm (divide the interception by the slope). Usually the interception should be positive due to the contamination, which can be seen from the alpha-fitting. If we want to get a more precise beta calibration line, the old phantom also needs further investigation. The intercept of the new phantom is -0.00590493 , which gives rise to a lead concentration of about -9ppm . It is obviously wrong.

Usually the phantoms for the calibration of the xrf measurement of lead in bone are made with plaster of Paris and they are usually being considered as having the same compositions. From the investigation, we can learn that their composition could be substantially different. So we should check the composition of the material before making the phantoms. Even for the current phantoms, we need to do some analysis to confirm their composition.

4.1 Conclusion for the improvement of the in vivo lead measurement system

The improvement of the MDL of the in vivo lead measurement system was investigated by both Monte Carlo simulation and the measurement. For a current source, the MDL of the in vivo measurement would be improved by a factor of 0.658 ± 0.049 compare to the standard system only by changing its geometry. The corresponding Monte Carlo simulation value is 0.681, which is quite close to the measurement value. If we use a cloverleaf system instead of the conventional system and use a stronger source (about 4.5 times stronger than the current source), and at the same time change the geometry to an optimal state, the value would be 0.278 ± 0.016 for the measurement and 0.273 for the Monte Carlo simulation, which is dramatic.

4.2 Conclusion for the lead measurement calibration

Two sets of phantoms were investigated and two important conclusions were obtained. One is that the difference between the calibration line of the old phantoms and the calibration of the new phantoms is due to the different composition of the phantoms. The smaller slope of the calibration lines for the new phantoms means that the ratio of the x-ray peak and coherent peak for a new phantom is bigger than that for an old phantom with the same concentrations. This means that there's more fraction of high Z elements in the new phantoms than that of the old phantoms. The negative intercept in the beta calibration line for the new phantoms is due to bigger concentration of Ca and smaller concentration of S in the new phantoms than that in the old phantoms. The ratio of $(S/Ca)_{old}/(S/Ca)_{new}$ was obtained by several methods and the value is around 2. The other

conclusion is that the ratio $Ca/(\text{coherent peak})$ has a linear relationship with the resolution of the system while the ratio $Ca/(\text{coherent peak} * \text{FWHM})$ is independent of the resolution.

4.3 Future work

In the first work, the cloverleaf system refers to a four 8 mm detectors system. But in the experiment, only one 12.5 mm detector covered by tin collimator was used to simulate the real system. So the future investigation for this work includes confirming the obtained results by a real cloverleaf system. In addition, measuring the bare phantom in a leg phantom, which is not a truly in vivo measurement, simulated the in vivo measurement in this work. Hence the in vivo measurement needs to be done in the future to examine the obtained results.

In the second work, since the chemical composition of the new phantom has not yet precisely determined, further analysis methods need to be used to solve this problem.

reference:

Ahlgren L, Lidén K, Mattsson S and Tejning S, X-ray fluorescence analysis of lead in human skeleton in vivo, *Scand. J. Work Environ. Health*, 1976, 2, pp82-86.

Ao Q, Lee S H, Gardner R P, Development of the specific purpose Monte Carlo code CEARXRF for the design and use of in vivo x-ray fluorescence analysis systems for lead in bone, *Appl Radiat Isot.* 1997 Oct-Dec, 48 (10-12), pp1403-1412 (a).

Ao Q, Lee S H, Gardner R P, Optimization of in vivo x-ray fluorescence analysis methods for bone lead by simulation with the Monte Carlo code CEARXRF, *Appl Radiat Isot.* 1997 Oct-Dec, 48 (10-12), pp1413-1423 (b).

Bateman S N, Pejovic-Milic A, Stronach I M, McNeill F E, Chettle D R, Performance appraisals of digital spectroscopy systems for the measurement of bone lead, *Appl Radiat Isot.* 2000 Oct-Nov, 53(4-5), pp647-650.

Bevington P R, *Data reduction and error analysis for the Physical Sciences*, 1969.

Börjesson J, Jonson R, Mattsson S, Muntving K, Tolli H, A Monte Carlo program for the determination of the optimum back scatter geometry when measuring mercury and other heavy metals in vivo, *Basic Life Sci.*, 1993 (60), pp267-273.

Chettle D R, Scott M C, and Somervaille L J, Lead in bone: sampling and quantitation using K x-rays excited by ^{109}Cd , *Environ Health Perspect* 1991, 91, pp49-55.

Environmental Health Criteria³, Lead, United Nations environmental program, World Health Organization, 1977.

Gordon C L, Chettle D R, Webber C E, An improved instrument for the in vivo detection of lead in bone, *British Journal of Industrial Medicine* 1993, 50, pp637-641.

Hoppin J A, Aro A C, Williams P L, Hu H, Ryan P B, Validation of K-XRF bone lead measurement in young adults, *Environ Health Perspect* 1995, 103(1), pp78-83.

Hoppin J A, Aro A, Hu H, Ryan P B, In vivo bone lead measurement in suburban teenagers, *Pediatrics*, 1997, 100(3 pt 1), pp365-370.

Leggett R W, An age-specific kinetic model of lead metabolism in humans, *Environmental Health Perspectives*, 1993 (101), No. 7, pp598-616.

McNeill F E, Stokes L, Chettle D R, Kaye W E, Factors affecting in vivo measurement precision and accuracy of ¹⁰⁹Cd K x-ray fluorescence measurements, *Phys Med Biol*, 1999, 44(9), pp2263-2273.

O'Meara J M, Chettle D R, McNeill F E, Prestwich W V, Sevansson C E, Monte Carlo simulation of source-excited in vivo x-ray fluorescence measurements of heavy metals, *Phys Med Biol.*, 1998 Jun, 43 (6), pp1413-1428).

O'Meara JM, Borjesson J, Chettle DR, Improving the in vivo x-ray fluorescence (XRF) measurement of renal mercury, *Appl Radiat Isot.*, 2000 Oct-Nov, 53 (4-5), pp639-646.

Ratcliffe J M, *Lead in man and the environment*, Chichester, Eng.: Ellis Horwood; New York: Halsted press, 1981.

Somervaille L J, Chettle D R and Malcolm C Scott, In vivo measurement of lead in bone using x-ray fluorescence, *Phys. Med. Biol.*, 1985, Vol. 30, No. 9, 929-943.

Stronach I M, McNeill F E, Chettle D R, O'Meara J M, Optimisation studies of in vivo lead measurement by x-ray fluorescence, presentation of Canadian Association of Physicists' Annual congress, York University, Toronto, Jan., 2000.

Todd A C, Chettle D R, Scott M C, Somervaille L J, Monte Carlo modeling of in vivo x-ray fluorescence of lead in the kidney, *Phys Med Biol*. 1991 Apr, 36 (4), pp439-448.

Todd A C, Chettle D R, In vivo x-ray fluorescence of lead in bone: review and current issues, Environ Health Perspect, 1994 Feb, 102 (2), pp172-177, Review.

[1] History of lead: Antiquity. [Http://members.aol.com/baltlead/HISTb.html](http://members.aol.com/baltlead/HISTb.html)

[2] ATSDR (Agency for Toxic Substances and Disease Registry) public Health Statement for lead. [Http://www.atsdr.cdc.gov/ToxProfiles/phs8817.html](http://www.atsdr.cdc.gov/ToxProfiles/phs8817.html)

[3] An assessment of the use of lead in electronic assembly. [Http://www.ipc.org/html/SMC.pdf](http://www.ipc.org/html/SMC.pdf)

[4] Case studies in Environmental Medicine: Lead Toxicity. ATSDR (Agency for Toxic Substances and Disease Registry). <http://www.atsdr.cdc.gov/HEC/caselead.html>